Supplementary Material for

Experimental and theoretical evidence of a supercritical-like transition in an organic semiconductor presenting colossal uniaxial negative thermal expansion

A. van der Lee, G. H. Roche, G. Wantz, J. J. E. Moreau, O. J. Dautel, J.-S Filhol

Other Supplementary Material for this manuscript includes:

Data (diffraction cif, fcf, and checkcif-files, *ab initio* molecular dynamics cif-files; the latter files are labeled alphaxK.cif and betaxK.cif where x is the temperature)

1. Diffraction and Crystallography

X-ray diffraction experiments

The synthesis of **BHH-BTBT** has been described in (*1*).

X-ray data for the structure were collected between 95 and 295 K in steps of 20K on a Rigaku Oxford Diffraction Gemini-S diffractometer with a Sapphire3 detector. Mo *Kα* radiation was used with a graphite monochromator and a fiber-optics Mo-Enhance collimator. The data integration, as well as the absorption and other corrections were carried with *CRYSALIS PRO* (*2*). Data were collected up to 99.9% completeness at 0.8 Å resolution and with a redundancy of 3.8. ω-scans were employed with a frame width of 1°, giving a total of 436 frames for each temperature. The structure was solved by iterative charge-flipping methods using *SUPERFLIP* (*3*). The structure refinements were carried out with *CRYSTALS* (*4*) and all non-hydrogen atoms were refined by non-linear full matrix least squares on F^2. Table S1 gives the experimental data and the results of the refinements for each temperature. All cif-and fcf-files and the corresponding checkcif reports are available as separate supplementary material to this publication. The cif-files corresponding to the ab initio DFT calculations are also available (labeled alpha0K.cif, beta235K.cif, etc; atomic coordinates for the latter are reported in the *P1* space group)

It is worthwhile noting that all unit cells have been chosen according to a body-centered *I* lattice. Due to the peculiar combination of the values of the cell axes and that of the monoclinic β angle, a *C*-centered cell could have been chosen as well. The convention is to use the centering which corresponds to the smallest β angle, but this would lead to a *C*-cell for the lowest temperatures and an *I*-cell for the highest temperatures. Even more confusing is that different *C*-centered cells are possible which is illustrated in scheme S1.
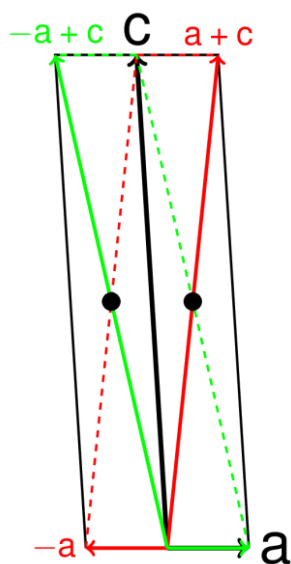
Scheme S1: Different choices for the unit cell of **BHH-BTBT**. The black cell corresponds to the *I*-centering with a β angle of approximately 95°, the red cell corresponds to a *C*-centering with a β angle of approximately 95°, and the green cell corresponds to a *C*-centering with a β angle of approximately 103°. The black dot corresponds to the centering and is in fact at *b*/2 perpendicular to the paper; it shows that the *I* centering is transformed in a *C*-centering.

The **P**-matrices to transform the *I*-centered cell into the two *C*-centered cells are (1 0 -1 / 0 1 0 / 1 0 0) and (-1 0 1 / 0 -1 0 / 1 0 0) for the red and green cells, respectively, where the transformation is defined as $(a_{new}, b_{new}, c_{new}) = (a_{old}, b_{old}, c_{old})$ **P**

Table S2 gives the cell parameters at 95 K and 295 K according to the different cell choices and notably the inversion of the β angle for the *I*-centered cell and the red *C*-centered cell.

	95K	115K	135K	155K	175K
formula	$C_{26}H_{32}O_2S_2$	$C_{26}H_{32}O_2S_2$	$C_{26}H_{32}O_2S_2$	$C_{26}H_{32}O_2S_2$	$C_{26}H_{32}O_2S_2$
moiety	$C_{26}H_{32}O_2S_2$	$C_{26}H_{32}O_2S_2$	$C_{26}H_{32}O_2S_2$	$C_{26}H_{32}O_2S_2$	$C_{26}H_{32}O_2S_2$
T (K)	95	115	135	155	175
spacegroup	$I2/a$	$I2/a$	$I2/a$	$I2/a$	$I2/a$
crystal system	monoclinic	monoclinic	monoclinic	monoclinic	monoclinic
a (Å)	7.7604(8)	7.8186(5)	7.8560(7)	7.9306(5)	7.9631(6)
b (Å)	5.9132(6)	5.8811(3)	5.8413(6)	5.8288(4)	5.8073(4)
c (Å)	49.450(4)	49.458(3)	49.561(4)	49.645(3)	49.723(3)
α (°)	90	90	90	90	90
β (°)	95.879(9)	95.762(6)	95.460(8)	95.171(5)	94.850(6)
γ (°)	90	90	90	90	90
V (Å³)	2257.3(2)	2262.64(14)	2263.98(18)	2285.51(14)	2291.14(15)
Z	4	4	4	4	4
ρ (gcm⁻³)	1.297	1.294	1.293	1.281	1.277
M_r (gmol⁻¹)	440.66	440.66	440.66	440.66	440.66
μ (mm⁻¹)	0.257	0.256	0.256	0.253	0.253
R_{int}	0.049	0.019	0.027	0.028	0.030
Θ (º)	29.075	27.721	27.231	27.819	29.180
resolution (Å)	0.73	0.767.7604	0.78	0.76	0.73
N_{tot} (measured)	9808	7900	6798	8237	10302
N_{ref} (unique)	2715	2324	2191	2376	2767
N_{ref} ($I>2\sigma(I)$)	2257	2140	1948	2012	2369
N_{ref} (least-squares)	2599	2286	2134	2271	2653
N_{par}	136	136	136	136	136
$<\sigma(I)/I>$	0.0518	0.0211	0.0326	0.0421	0.0359
R_1 ($I>2\sigma(I)$)	0.0520	0.0296	0.0339	0.0354	0.0353
wR_2 ($I>2\sigma(I)$)	0.0619	0.0624	0.0776	0.0519	0.0809
R_1 (all)	0.0641	0.0326	0.0391	0.0442	0.0427
wR_2 (all)	0.0707	0.0651	0.0840	0.0625	0.0868
GOF	1.1160	0.9209	0.9222	0.9734	0.8841
$\Delta\rho$ (eÅ⁻³)	-0.77/0.41	-0.22/0.25	-0.23/0.25	-0.20/0.26	-0.23/0.30
crystal size (mm³)	0.30x0.35x0.40	0.30x0.35x0.40	0.30x0.35x0.40	0.30x0.35x0.40	0.30x0.35x0.40

	195K	215K	235K	255K	275K	295K
formula	$C_{26}H_{32}O_2S_2$	$C_{26}H_{32}O_2S_2$	$C_{26}H_{32}O_2S_2$	$C_{26}H_{32}O_2S_2$	$C_{26}H_{32}O_2S_2$	$C_{26}H_{32}O_2S_2$
moiety	$C_{26}H_{32}O_2S_2$	$C_{26}H_{32}O_2S_2$	$C_{26}H_{32}O_2S_2$	$C_{26}H_{32}O_2S_2$	$C_{26}H_{32}O_2S_2$	$C_{26}H_{32}O_2S_2$
T (K)	195	215	235	255	275	295
spacegroup	$I2/a$	$I2/a$	$I2/a$	$I2/a$	$I2/a$	$I2/a$
crystal system	monoclinic	monoclinic	monoclinic	monoclinic	monoclinic	monoclinic
a (Å)	8.0248(6)	8.0891(6)	8.1615(7)	8.2606(6)	8.3546(5)	8.4460(3)
b (Å)	5.7688(5)	5.7282(4)	5.6918(5)	5.6541(3)	5.6236(3)	5.58942(19)
c (Å)	49.827(4)	49.849(4)	49.870(4)	49.944(3)	50.168(3)	50.2534(15)
α (º)	90	90	90	90	90	90
β (º)	94.591(7)	94.255(6)	93.819(7)	93.621(6)	93.146(5)	92.829(3)
γ (º)	90	90	90	90	90	90
V (Å³)	2299.26(18)	2303.46(19)	2311.5(2)	2328.04(15)	2353.50(12)	2369.48(7)
Z	4	4	4	4	4	4
ρ (gcm^{-3})	1.273	1.271	1.266	1.257	1.244	1.235
M_r (gmol^{-1})	440.66	440.66	440.66	440.66	440.66	440.66
μ (mm^{-1})	0.252	0.251	0.251	0.249	0.246	0.244
R_{int}	0.027	0.022	0.021	0.020	0.022	0.028
Θ_{max} (º)	27.745	27.948	27.779	27.949	27.826	27.910
resolution (Å)	0.76	0.76	0.76	0.76	0.76	0.76
N_{tot} (measured)	7616	7662	7686	7663	8011	20985
N_{ref} (unique)	2351	2362	2371	2411	2431	2631
N_{ref} ($I>2\sigma(I)$)	2117	2106	2093	2104	2017	2345
N_{ref} (least-squares)	2297	2288	2299	2322	2325	2566
N_{par}	136	136	136	136	136	136
$<\sigma(I)/I>$	0.0314	0.0275	0.0280	0.0278	0.0309	0.0252
R_1 ($I>2\sigma(I)$)	0.0326	0.0325	0.0339	0.0359	0.0368	0.0361
wR_2 ($I>2\sigma(I)$)	0.0603	0.0711	0.0778	0.0630	0.0541	0.0876
R_1 (all)	0.0366	0.0373	0.0394	0.0427	0.0471	0.0407
wR_2 (all)	0.0667	0.0773	0.0830	0.0696	0.0603	0.0972
GOF	0.9514	0.8551	0.8332	0.9880	0.9597	0.7832
$\Delta\rho$ (eÅ^{-3})	-0.22/0.23	-0.23/0.23	-0.20/0.24	-0.16/0.21	-0.21/0.17	-0.19/0.22
crystal size (mm³)	0.30x0.35x0.40	0.30x0.35x0.40	0.30x0.35x0.40	0.30x0.35x0.40	0.30x0.35x0.40	0.30x0.35x0.40

Table S1 : Crystal, diffraction, and refinement data for the structure of **BHH-BTBT**.

	95 K - *a* (Å) - 295 K		95 K - *b* (Å) - 295 K		95 K - *c* (Å) - 295 K		95 K - β (°) - 295 K	
I-centering	7.7604	8.4460	5.9132	5.5894	49.4500	50.2533	95.879	92.829
C-centering	49.2637	50.5454	5.9132	5.5894	7.7604	8.4460	93.136	96.778
C-centering	50.8344	51.3677	5.9132	5.5894	7.7604	8.4460	104.614	102.281

Table S2 : Cell parameters of the structure of according to the different choices for the unit cell at 95 K and 295 K.

General description of the structure of BHH-BTBT

Fig. S1 gives projections of the **BHH-BTBT** structure down the *a* and *b*-axes. The structure is best described as a dense packing of **BHH-BTBT** layers along the *c*-axis. The layers are separated by a hydrogen-bonded network parallel to the *ab*-plane. Most of the structural drawings in this supplementary material and in the main manuscript have been made with the *OLEX2* software (*5*) and some with *VESTA* (*6*).

Hydrogen bond network in BHH-BTBT

A particular structural feature is the hydrogen-bond connected space between two layers (Fig. S2). Each hydroxyl group has two possible orientations in the centrosymmetric space group *I*2/*a*, but locally only one orientation is possible, such that in the interlayer space hydrogen bonded zigzag chains run parallel to each other, either with the same or in opposite polar conformations or even with random polarities. The X-ray diffraction data do not permit to distinguish between the centrosymmetric space group *I*2/*a* and the non-centrosymmetric space group *Ia* with the same reflection extinctions, because of the very low anomalous scattering at the used wavelength.
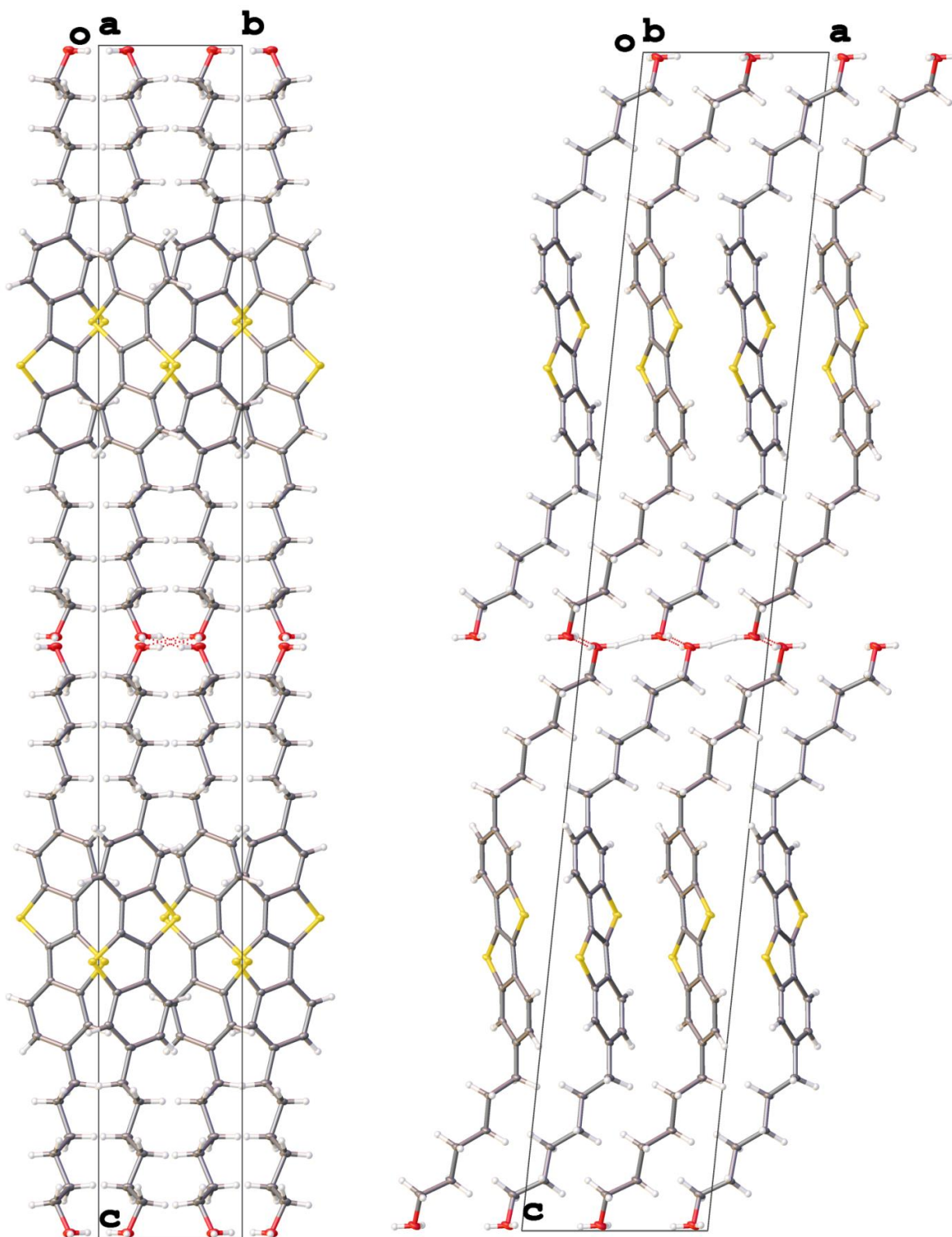
Fig. S1 Projection of the structure down a (left) and b (right) at 95K. Atomic displacement ellipsoids have been drawn at the 50% probability level.
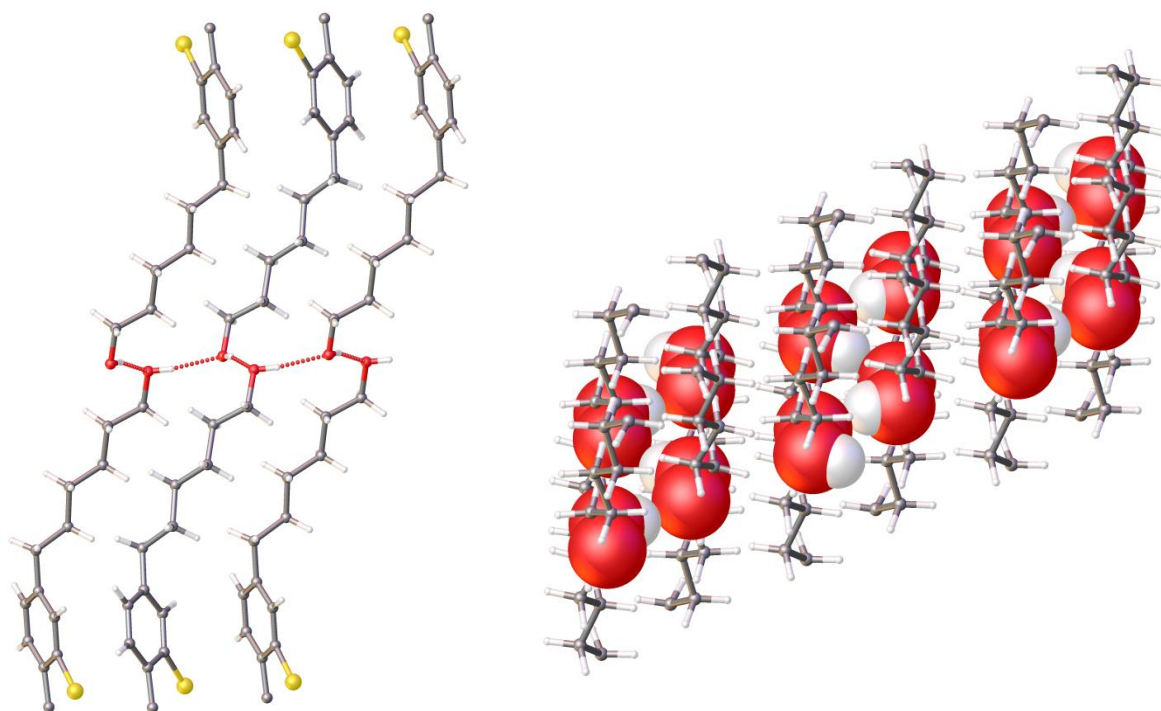
Fig. S2 : Left – single hydrogen-bonded zigzag chain in the interlayer space of the title compound. Right: parallel anti-phase zigzag hydrogen-bonded chains in the interlayer space of the title compound. The chains have been arbitrarily cut for more visibility in the interlayer space.

Fig. S3 gives a more detailed view of the hydrogen bonded network. The network is not two-dimensional, but consists of parallel infinite one-dimensional hydrogen-bonded chains. The chains are nearly parallel to the a-axis, making an angle of 0.96° at 95 K and 1.37° at 295 K. The oxygen sub-lattice is in fact slightly puckered as can be seen in the projection along the *b*-axis.
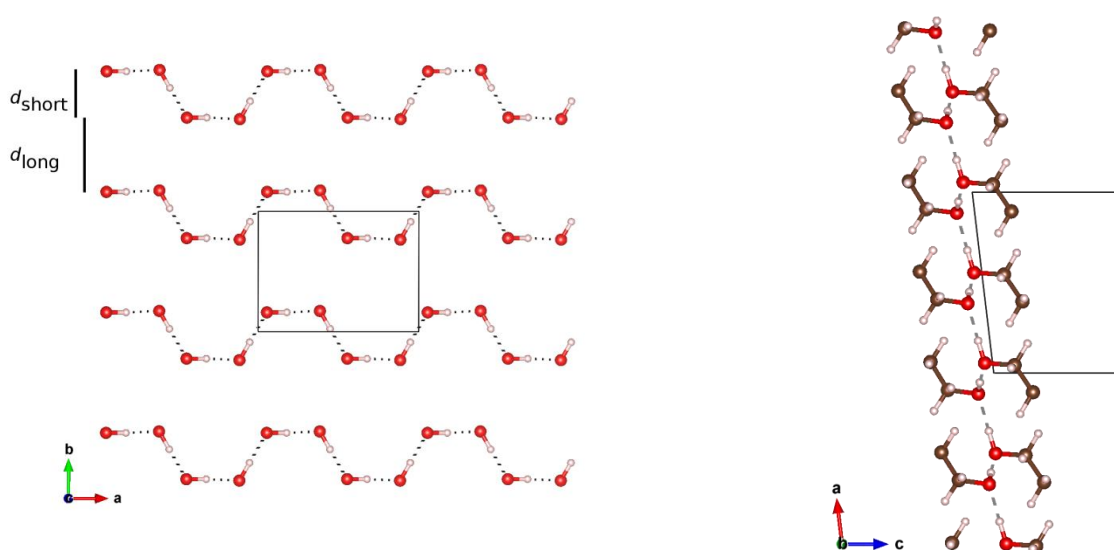
Fig. S3 : Projection of the hydrogen bonded network on the (001) plane (left); projection of the hydrogen bond network on the (010) plane (right). Hydrogen bonds are indicated by dashed lines. The straight black lines indicate the outline of the unit cell.

Fig. S4 and Fig. S5 give the evolution of the hydrogen-bonded network as a function of temperature. The DFT structures were used for the $O \cdots H$ distances and $H \cdots OH$ angles in Fig. S4, since the disorder in the hydrogen-bonded network does not permit to extract reliable values from the experimental data. The acceptor-donor $O \cdots O$ distances in Fig. S6 were extracted from the experimental X-ray data. It is clear that the expansion of the hydrogen-bonded network is directly related to the positive and negative thermal expansion in the *ab*-plane. One $O \cdots H$ intermolecular vector is nearly co-linear with the *a*-axis, which displays a large positive expansion, whereas the other is approximately aligned with *b-a*. This gives an overall net expansion of the $O \cdots H$ distance of about 3% between 0 K and 295 K. The DFT simulations show in addition that the disorder as observed in the hydrogen-bonded network by the X-ray structural determinations is of a static nature, and not dynamic (JSF, detail please, here or in the DFT section). The intra-chain perpendicular distance d_{short} (Fig. S3) contracts as a consequence as a function of temperature, whereas the inter-chain perpendicular distance d_{long} remains nearly constant as a function of temperature (Fig. S6).
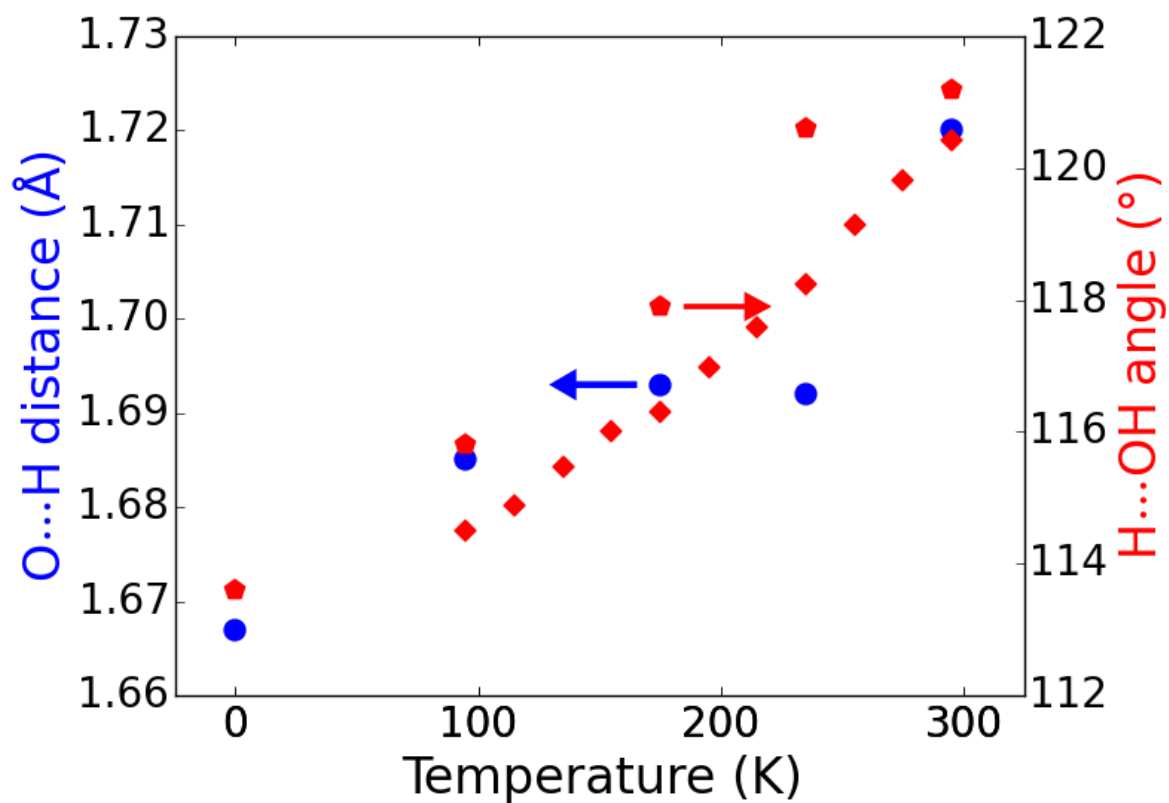
Fig. S4 : Intermolecular O⋯H distances (blue dots) and H⋯OH angles (red pentagons) in the structure of **BHH-BTBT** as a function of temperature as derived from the DFT calculations. The red diamonds give the corresponding O(H)⋯O(H)⋯O angles derived from the x-ray data. These angles are not necessarily identical to the H⋯OH angles, but appear to correspond pretty well.
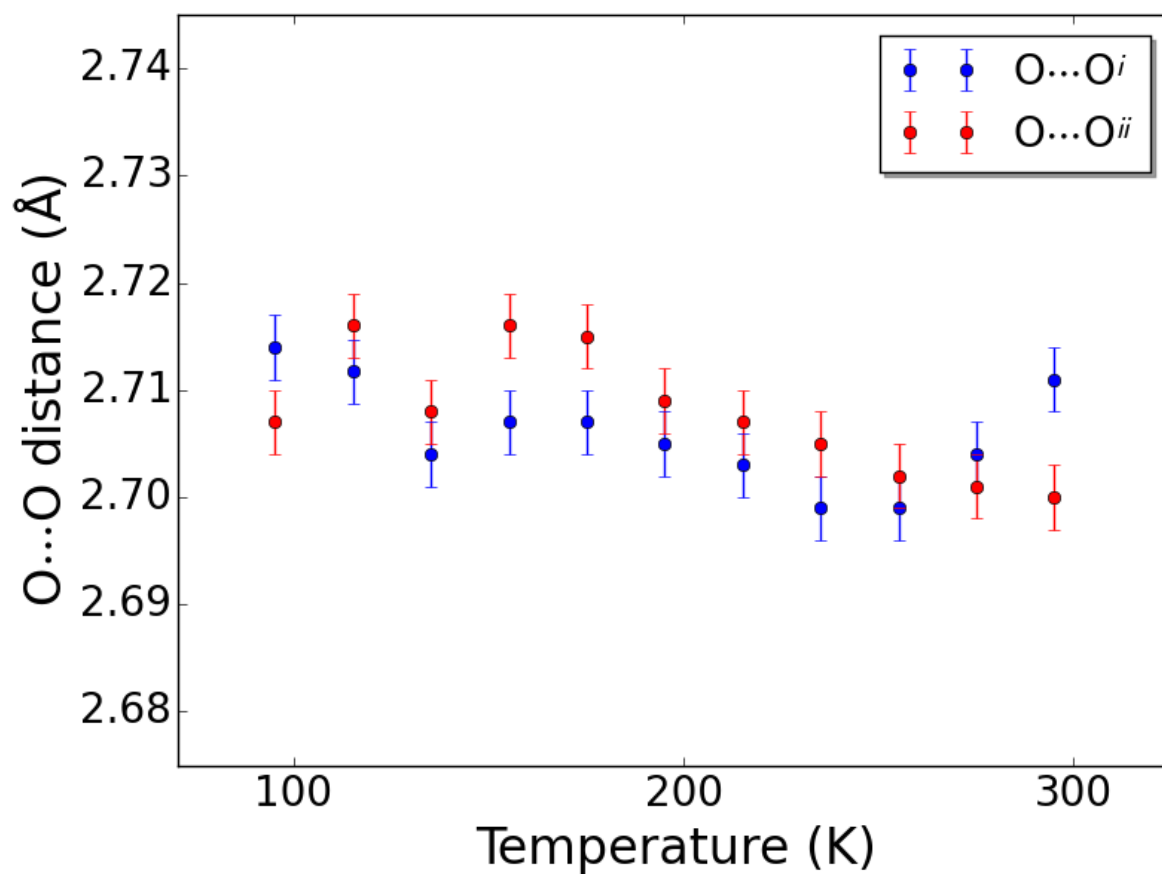
Fig. S5: Intermolecular O···O acceptor-donor distances as a function of temperature as calculated from the X-ray structures. Symmetry codes: *i* 2-*x*,1-*y*,1-*z*; *ii* 5/2+*x*,*y*,1-*z*
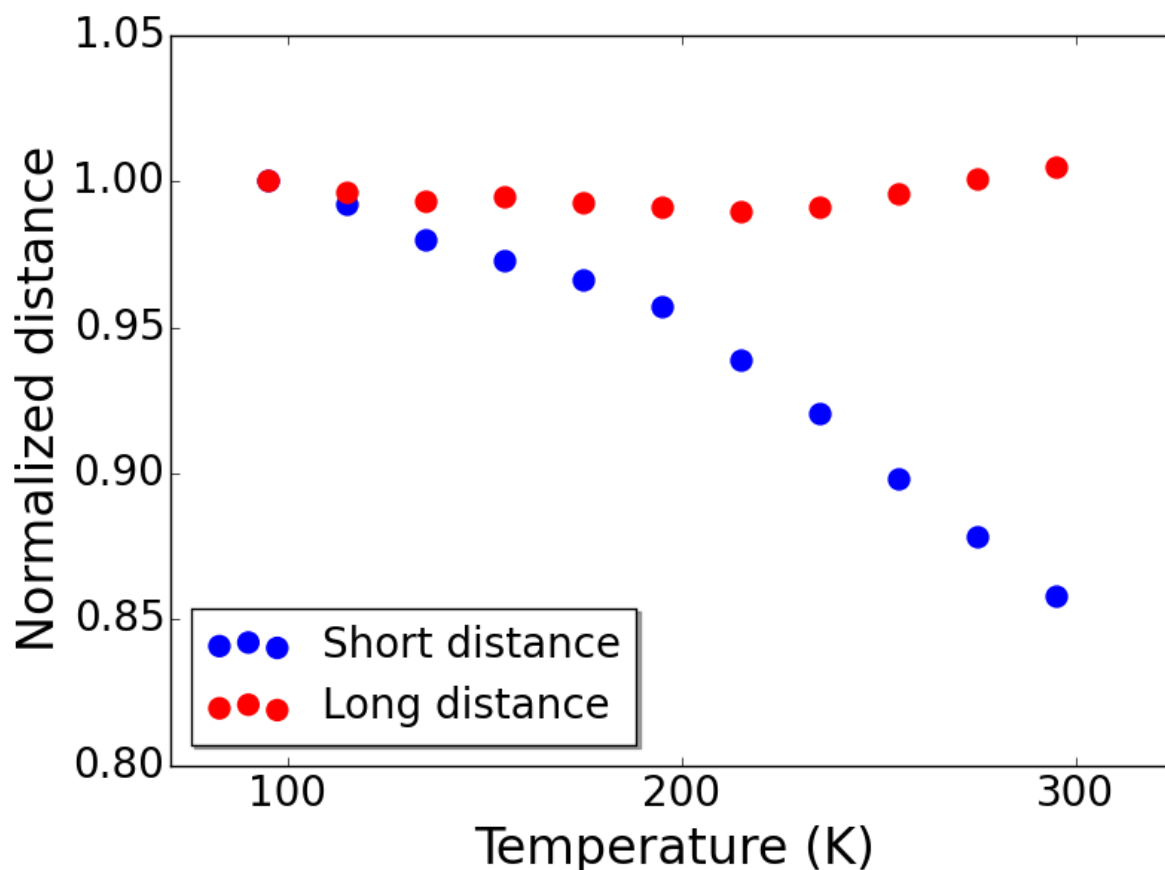
Fig. S6: Normalized distances between parallel lines within the zig-zag hydrogen-bonded 1D chain (blue dots) and between parallel chains (red dots, see **Fig. S3**)

Modeling of the thermal expansion

The empirical fitting method proposed by Ogborn *et al.* (*7*) was used to model the thermal expansion of **BHH-BTBT**. The thermal expansion is never truly linear and for this reason an empirical expression of the form

$$x(T) = x_0 + \kappa T \left(\frac{T}{T - T_c}\right)^{\lambda}$$ **Eq. 1**

is used with four fitting parameters. The fit was performed with the curve_fit module of the Python SciPy library. The fitted curves are shown in Fig. S7.
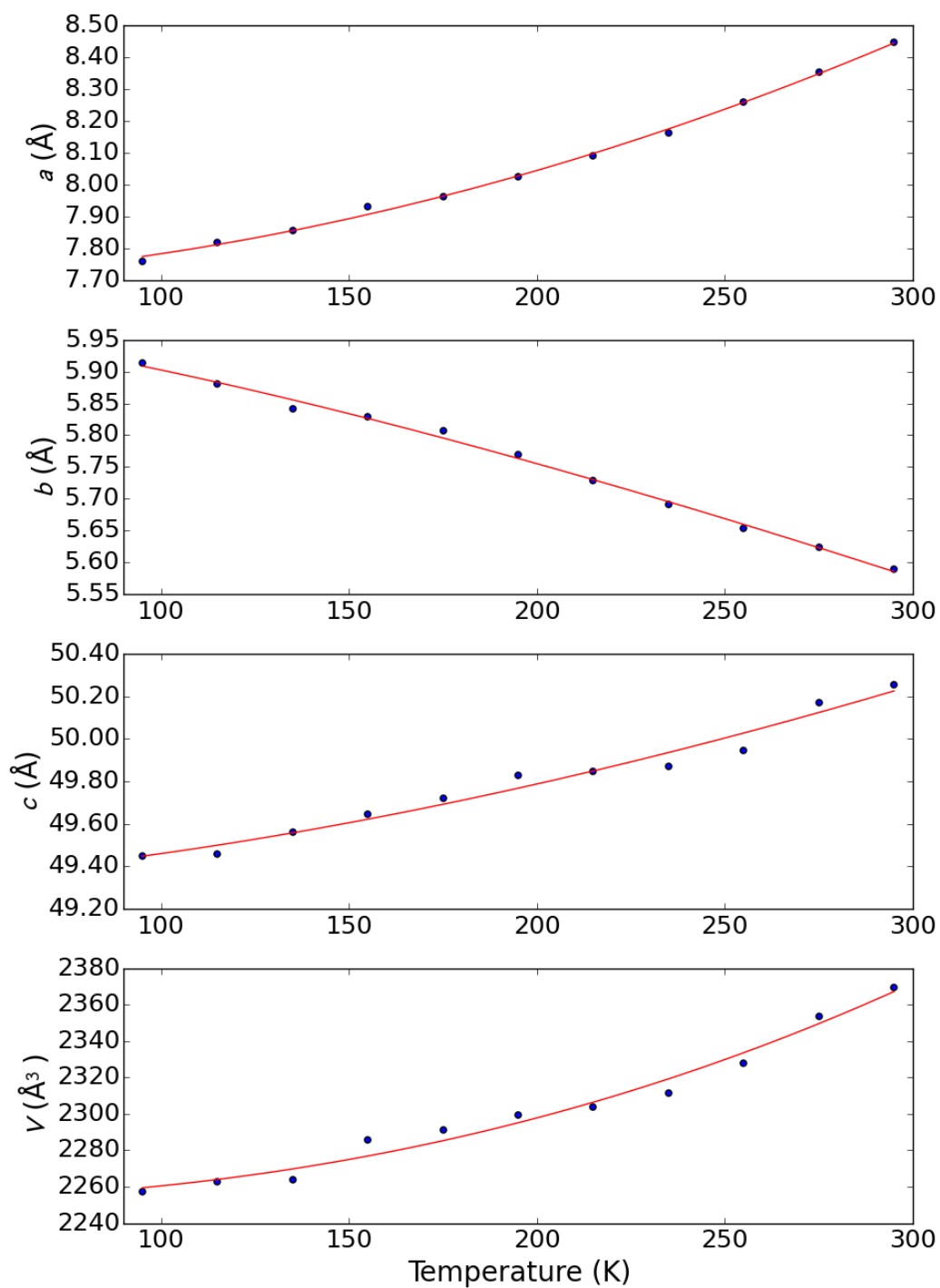
Fig. S7 : Non-linear fits to the experimental lattice parameter data as a function of temperature.

In order to calculate the thermal expansivity:

$$\alpha_l = \frac{1}{l}\left(\frac{\partial l}{\partial T}\right)$$

Eq. 2

for $l=\{a, b, c, V\}$ the derivative of the empirical expansivity curve was calculated using the analytical formula:

$$\frac{\partial l}{\partial T} = \frac{\kappa(T - T_c(\lambda+1))\left(\frac{T}{T-T_c}\right)^{\lambda}}{T - T_c}$$

<div align="right">**Eq. 3**</div>

which results in the thermal expansion curves in Fig. S8.
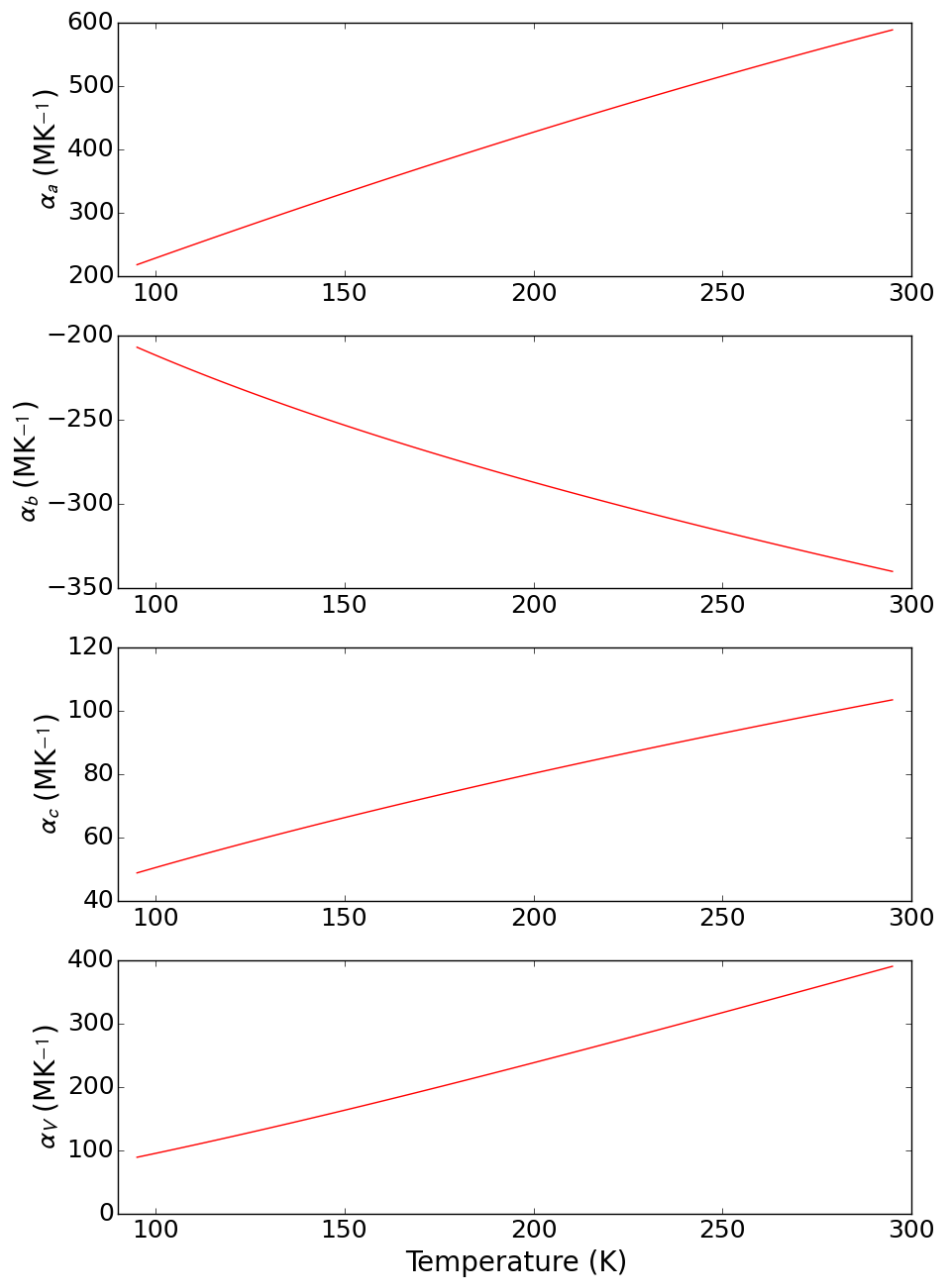
Fig. S8 : Calculated thermal expansivities as a function of temperature using the experimental fits to the experimental lattice parameters.

A space group independent way to describe the thermal expansivity is by the determination of the isobaric thermal expansion tensor, which is expressed in an orthogonal reference system, in contrast to the thermal expansion coefficients which are calculated along the crystallographic axes. The latter

method makes the comparison with other systems more difficult. From the isobaric thermal expansion tensor the direction and the magnitude of the thermal expansion ellipsoid main axes can be calculated via the principal axes and the eigenvalues of the tensor. It is expected that a deformation of a structure by an external parameter such as the temperature will be maximal there where the interactions are minimal. The eigenvalues of the tensor give therefore an idea about the directions of the weakest and the strongest interactions in the structure (*8*), (*9*). Fig. S9 gives the eigenvalues of the unit strain tensor of the thermal expansion tensor as a function of temperature. The eigenvalues were calculated using the modeled cell parameters in Fig. S7 with the *STRAIN* module of the *PLATON* program (*10*).
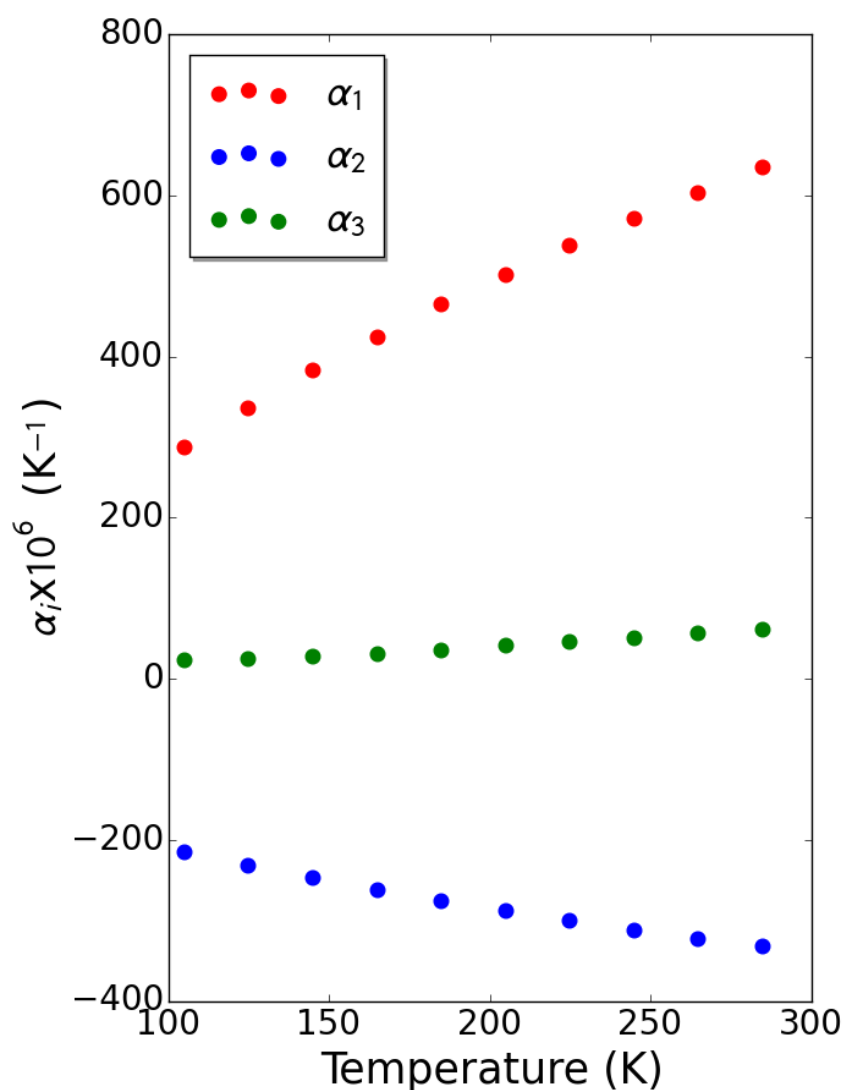
Fig. S9 : Eigenvalues of the unit strain tensor of the thermal expansion for **BHH-BTBT** as a function of temperature

As expected NTE is strictly perpendicular to the *ac*-plane and thus parallel to the *b*-axis. The lowest positive thermal expansion occurs along a direction making an angle of 107-115° with the *a*-axis and 14-19° with the *c*-axis. The strongest positive thermal expansion encloses an angle of 17-25° with the crystallographic *a*-axis and 70-75° with the *c*-axis.

Fig. S10 shows the expansivity indicatrix of **BHH-BTBT**, i.e. the surface that gives the magnitude of the thermal expansion α along a certain direction r, where the red surface represents positive thermal expansion and the blue surface negative thermal expansion (*11*). The principal axes are the orthogonal axes along which the crystal contracts or expands linearly. The advantage of the expansivity indicatrix over the usual strain ellipsoid is that with the former representation large positive and negative expansivities are more easily identified.
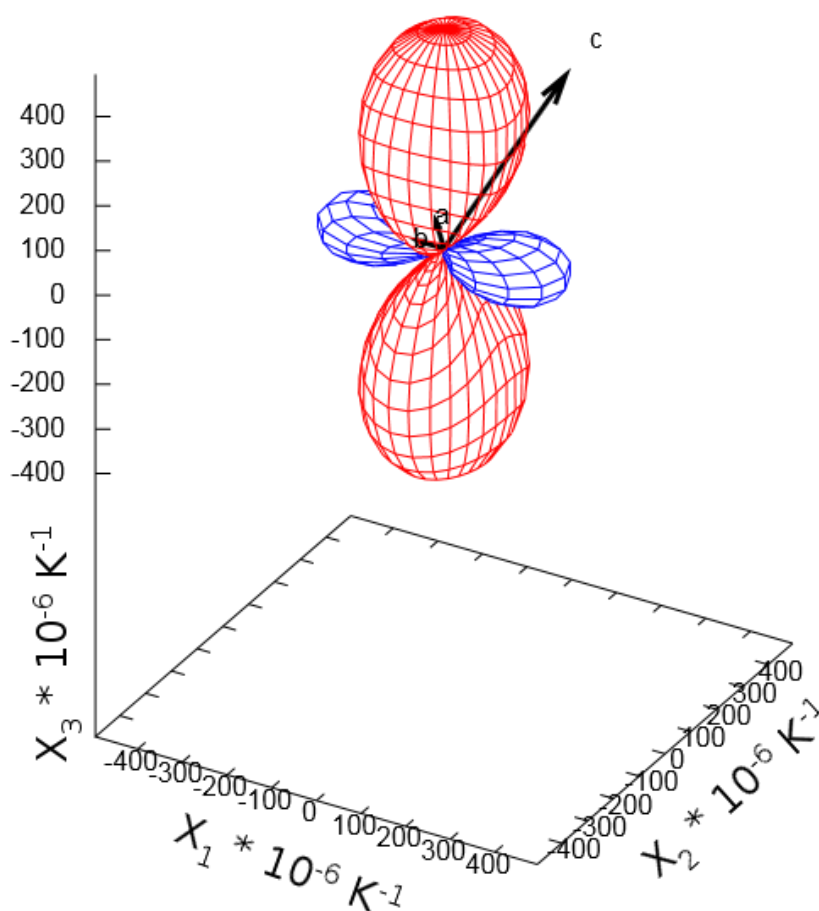
Fig. S10: Expansivity indicatrix of **BHH-BTBT**; the monoclinic crystal axes are represented by three vectors *a*, *b*, and *c*.

The principal axis X_1 indicates the strongest negative thermal expansion that is strictly collinear with the crystallographic *b*-axis, whereas the two principal axes X_2 and X_3 are approximately along [-2 0 1] and [15 0 1], respectively.

In order to verify whether the large observed positive thermal expansion is due to the opening of the herringbone angle as a function of temperature, the hypothetical thermal expansion due to this opening was calculated from

$$\alpha_{her} = \frac{1}{\left(\sin\left(\theta_1/_2\right)+\sin\left(\theta_2/_2\right)\right)/2} \frac{\sin\left(\theta_2/_2\right)-\sin\left(\theta_1/_2\right)}{20}$$ **Eq. 4**

Where 20 refers to the experimental temperature interval ΔT and Θ_1 and Θ_2 are the herringbone angles at two successive temperatures. The direction of this thermal expansion was determined to be along the normal vector of the bisector plane of the two least-squares planes going through the non-hydrogen atoms of the **BTBT** core. The experimental thermal expansion in the same direction was determined from the isobaric thermal expansion tensor interpolated at temperatures halfway two experimental temperature points.
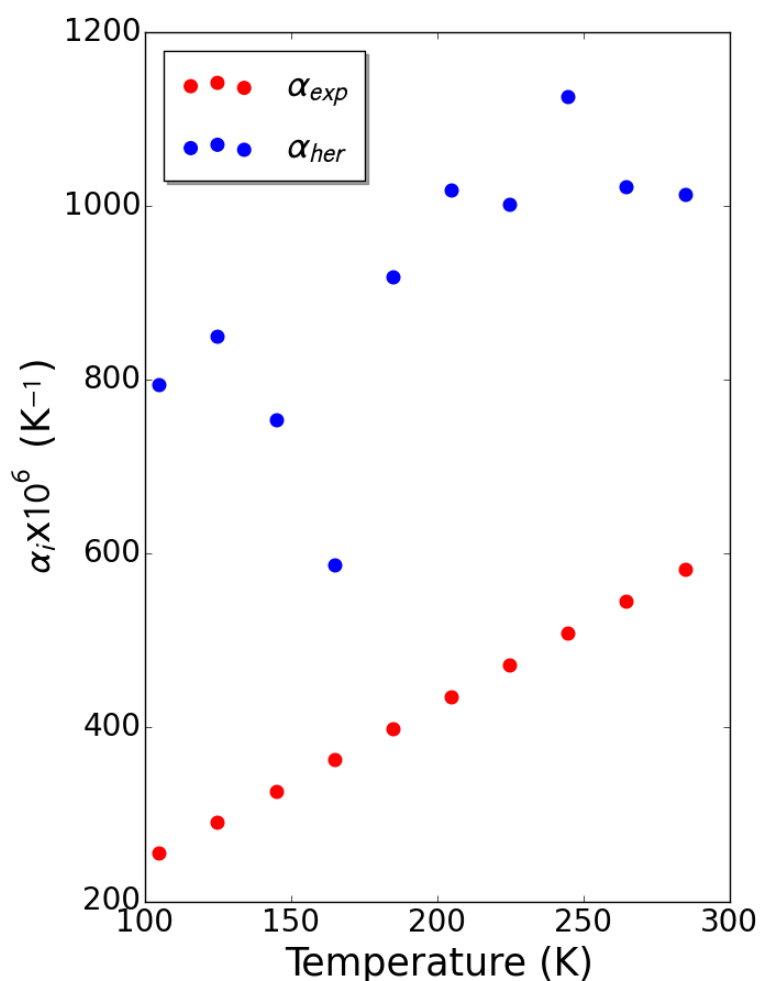
Fig. S11: Hypothetical thermal expansion due to the opening of the herringbone angle as a function of temperature and experimental thermal expansion in the same direction.

Fig. S11 gives the hypothetical and expansion thermal expansion as a function of temperature. The spread for the hypothetical thermal expansion data points is rather large. This is a consequence of the subtraction of two close values in the nominator of Eq. 3. The main conclusion if that the hypothetical thermal expansion is much larger than the experimental thermal expansion. This is exactly the opposite from what is observed in acenes, where the hypothetical thermal expansion is smaller than the observed one. This result could be anticipated from the difference temperature behavior of the herringbone angle in acenes and in **BHH-BTBT**: an increase of 0.3-1° over 100K in acenes versus 5-7° in **BHH-BTBT**.

TLS motion determination in BHH-BTBT

To further analyze the correlated movements of the molecules in **BHH-BTBT** a TLS analysis was carried out. Molecules are in such a description represented as rigid bodies. Thermal expansion is closely connected to the correlated movements of these rigid bodies; it can be shown that the amplitudes of the intramolecular modes are much smaller than those of the rigid bodies (*12*). The rigid body motion itself is described by three eulerian angles and a position vector and its motion by a translation T tensor, a librational L tensor, and a coupling tensor S within the molecular inertial system I. The 20 TLS parameters are derived from the observed atomic displacement parameters of the individual atoms making up the rigid body (*13*), (*14*). Fig. S12 plots the eigenvalues of I, T and L as a function of temperature; the coupling tensor S is equal to the zero tensor for all temperatures. The tensor of inertia I gives an idea how the mass is distributed in the rigid body. Since the three eigenvalues of I are essentially independent of the temperature, this shows that the internal conformation of the molecule hardly changes as a function of temperature which corroborates the results of several measurements of intramolecular angles as a function of temperature (Fig. S13). The anisotropy of the eigenvalues reflects the stretched geometry of **BHH-BTBT**. The eigenvector corresponding to the smallest eigenvalue of I, I_1 has an angle mismatch of approximately 5° with the crystallographic *c*-axis and is thus approximately aligned with the long molecular axis of **BHH-BTBT**.

In contrast to the tensor of interia, the librational and translational parameters do show a dependency on temperature. The eigenvector of the largest L_1 eigenvalue, has an angle mismatch of about 5° (at 295 K) up to 10° (at 95 K) with the molecular axis that is nearly aligned with I_1.
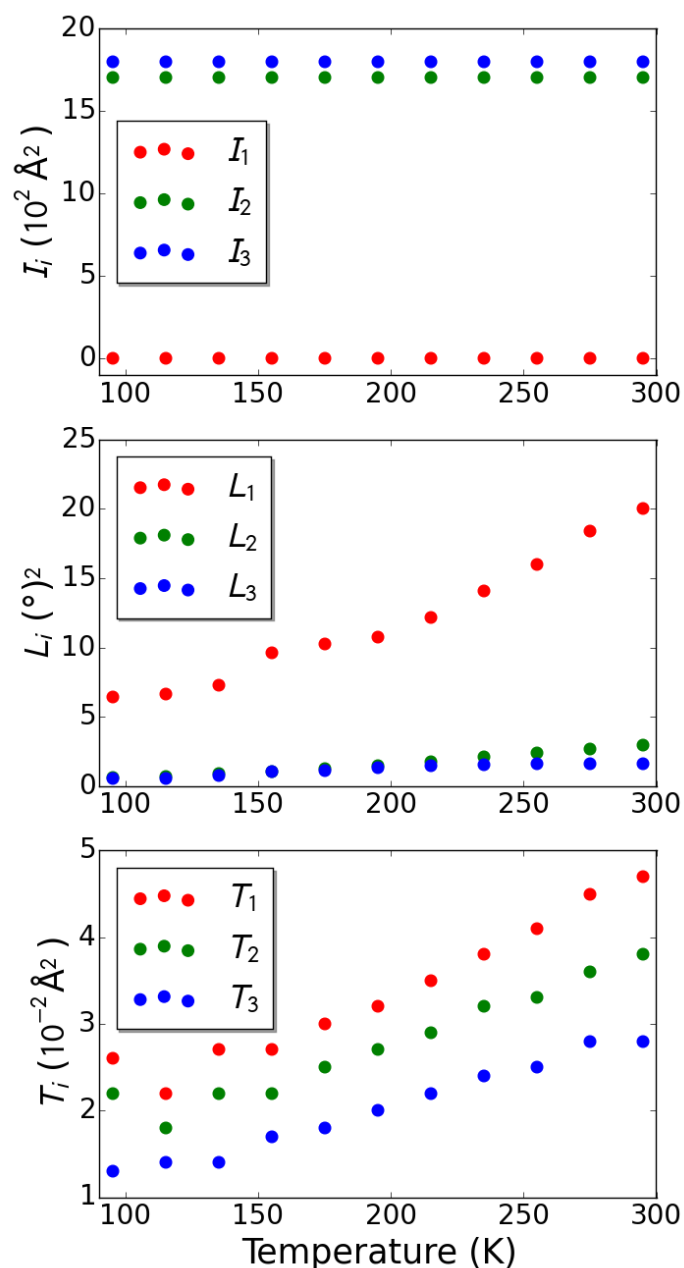
Fig. S12: Eigenvalues of the tensor of inertia *I*, upper plot; the librational tensor *L*, middle plot; the translational tensor *T*, bottom plot, for a rigid-body description of **BHH-BTBT** as a function of temperature. *I* is expressed in a Cartesian coordinate system and *L* and *T* in the inertial system *I*.

Additional temperature dependent geometrical parameters

In Fig. S13 the temperature dependence of the intramolecular geometry is reported. Angle 1 refers to the angle between the least-squares plane through the non-hydrogen atoms of the **BTBT** core and the line connecting atoms O15 and C7, which is in fact the angle between this line and the normal of the least-squares plane (Fig. S14). Angle 2 is the angle between the least-squares plane through the non-hydrogen atoms of the **BTBT** core and the least-squares plane of the non-hydrogen atoms of the

hydroxy-hexyl chain attached to the benzo moiety of the **BTBT** core (Fig. S14). It is easily observed that the both angles are essentially temperature independent, showing that the internal conformation of the **BHH-BTBT** molecules hardly change with temperature.
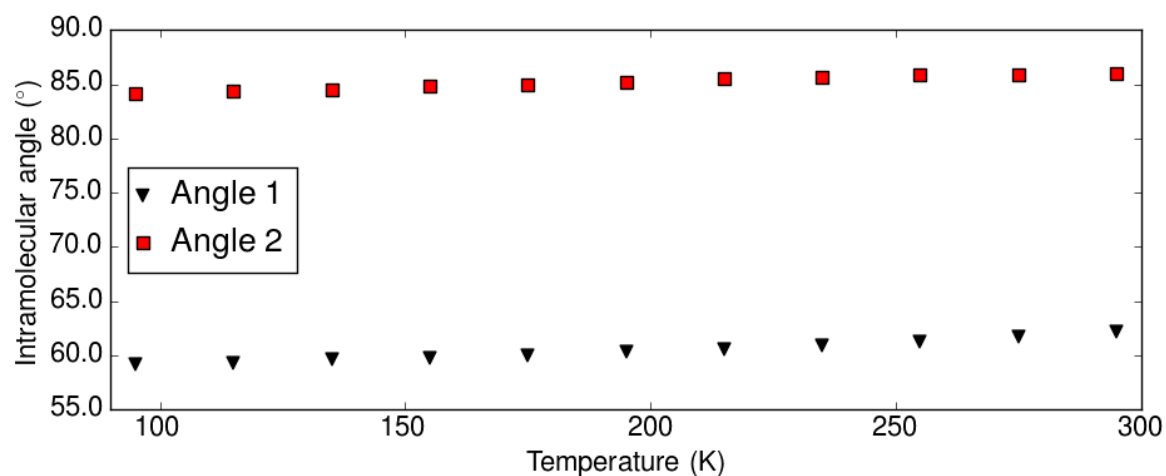
Fig. S13: Intramolecular angles 1 and 2 as a function of temperature (see for a definition of angles 1 and 2 Fig. S15)
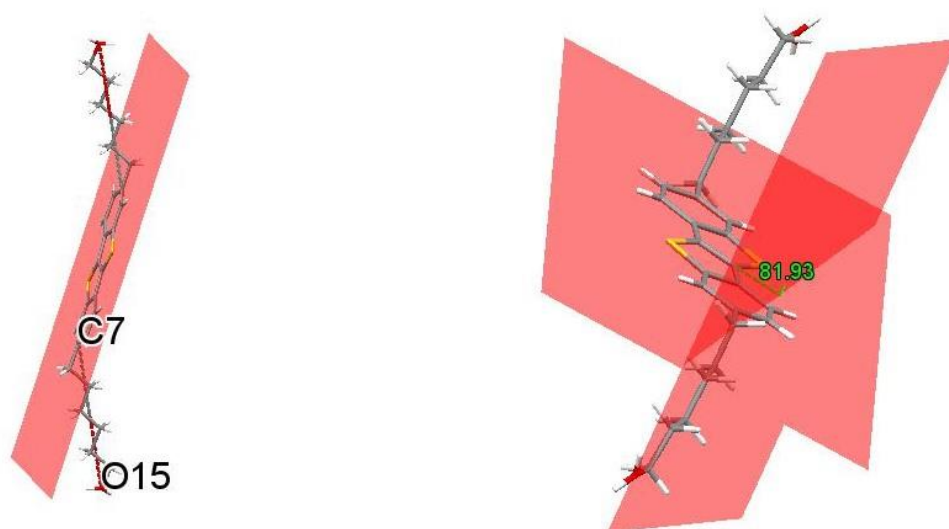
Fig. S14: Definition of intramolecular angles 1 and 2 (see caption Fig. S14). Angle 1 is the angle between the least-squares plane of the BTBT core and the straight line between atom C7 and O15. Angle 2 is between the least-squares plane of the BTBT core and the least-squares plane of all non-hydrogen atoms of a side chain.
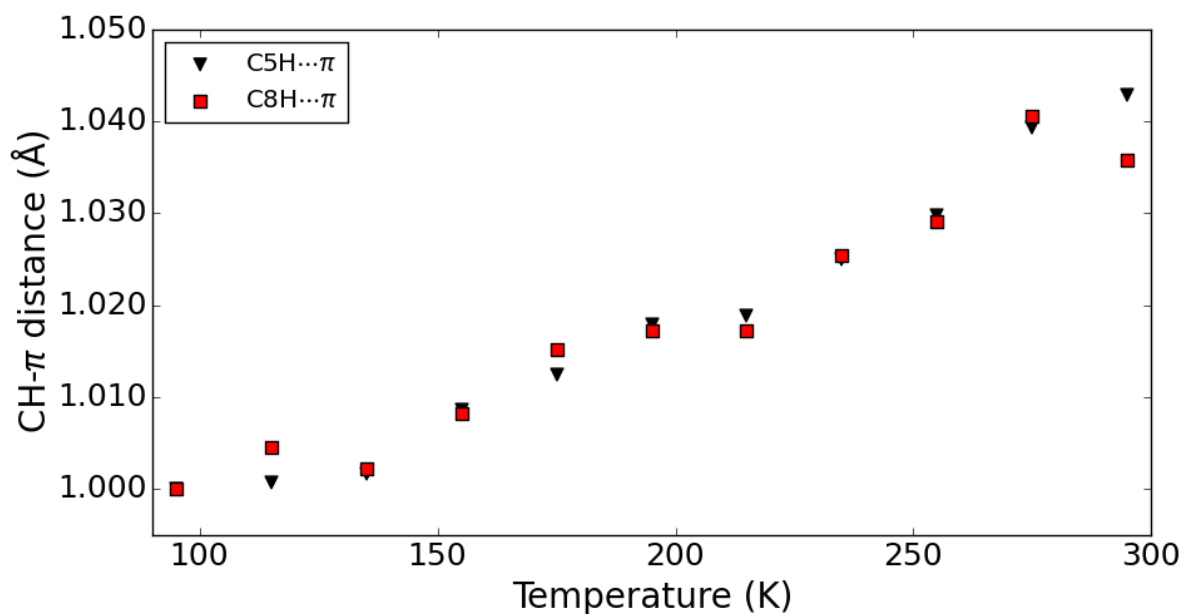
Fig. S15: CH···π angles as a function of temperature. The two different angles are depicted in Fig. S17.
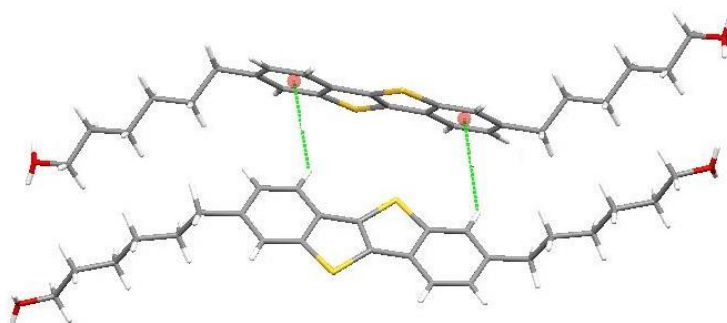
Fig. S16: Very weak CH···π interactions in the structure of **BHH-BTBT**.

Fig. S15 gives the temperature dependence of CH···π interaction distances, it should be noted that these CH···π interactions are probably weaker than the S···S and S···C interactions, because they are slightly larger than 3.0 Å (Fig. S16). The interaction is slightly better between the two CH groups and the aromatic carbons common to the thiophene and the benzo moiety. The temperature dependency is quite normal with a slight tendency to stagnation between 95 K and 150 K, which does not correspond to the approximate phase transition temperature observed from the DFT calculations and the temperature dependency of the S···C contact distance.

Cambridge Structural Database survey

Three different queries in the Cambridge Structural Database (*15*) were performed: on structures with

Scheme S2: structures with **BTT** (left) and **BTBT** (right) cores

bisthieno-thiophene (**BTT**) and a benzothieno-benzothiophene (**BTBT**) core (Scheme S2) in particular on structures with close thieno-thiophene cores (centroid to centroid distance below 6.0 Å). For the **BTT** and **BTBT** searches co-crystal structures, i.e. crystal structures containing other molecules without **BTT** or **BTBT** cores in the unit cell and structures with disordered fragments were excluded from the search results. Different geometrical parameters were determined: the tilt angle between two adjacent **BTT** of **BTT** cores in face-edge (FE) orientation (see Fig. S17),
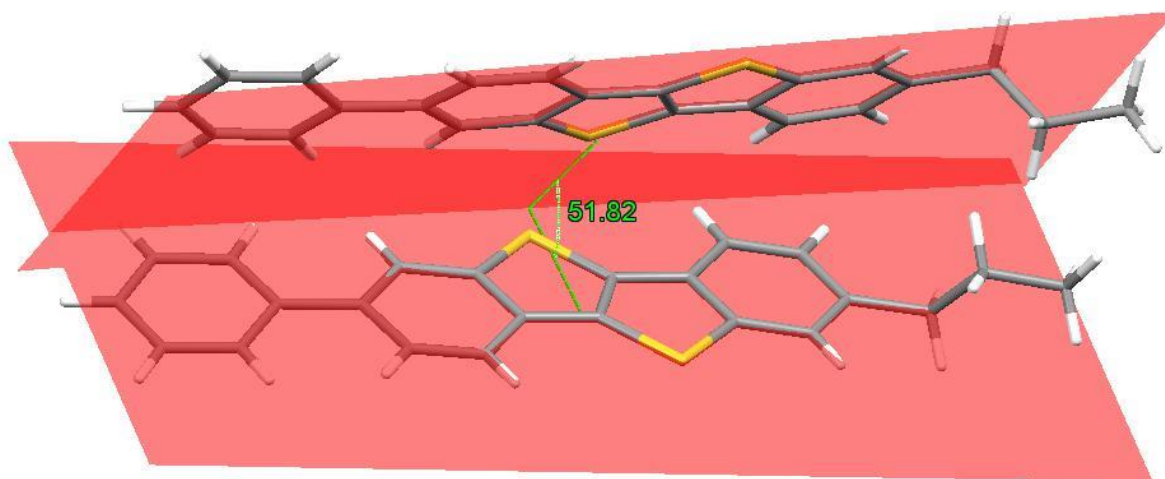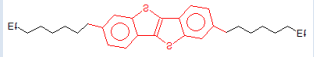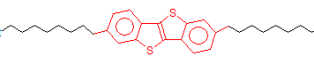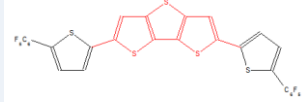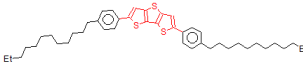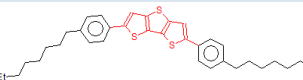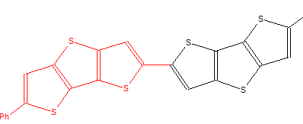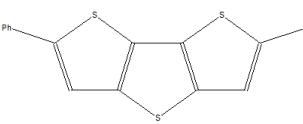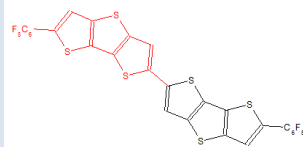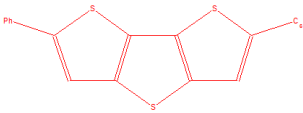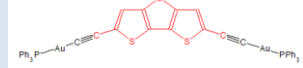

Fig. S17 : Tilt or herringbone angle between adjacent **BTT** of **BTBT** cores in face-edge (FE) orientation. The depicted molecule is 2-phenyl-7-propyl[1]benzothieno[3,2-b][1]benzothiophene, CSD refcode DURMUA.

and the shortest S⋯S and S⋯C distances in FF and EE orientations. Table S3 compiles the results.

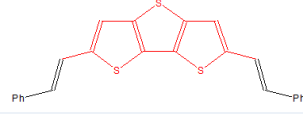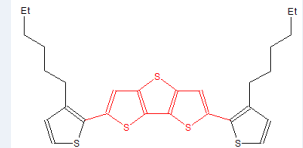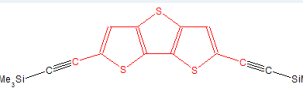| CSD refcode	orien-tation	S···S (FE/EE,Å)	S···C (Å)	angle (°)	T (K)	Scheme
BTBT						
DURMUA	FE/EE	3.70/3.60	3.49/3.45	51.8	300	
DURNAH	FE/EE	-/3.58	3.43/3.45	53.9	300	
DURNEL	FE/EE	3.78/3.57	3.49/3.56	51.0	300	
DURNIP	FE/EE	3.79/3.60	3.48/3.52	51.7	300	
DURNOV	FE/EE	3.79/3.57	3.46/3.51	49.9	300	
ILUTAM	FE/EE	-/3.53	3.61/3.62	53.4	123	
KUDFAS	FE/EE	-/3.78	3.55/3.80	53.3	123	
PIVBAY	FE/EE	3.62/3.54	3.41/3.42	54.0	300	
ROQSAT	FE/EE	3.75/3.54	3.41/3.44	48.5	300	
UROBUA	FE/EE	/3.53	3.43/3.32	64.9	295	
UVAHEF	FE/EE	3.95/3.51	3.41/3.48	42.3	300	

YOKBIK	FE/EE	3.67/3.61	3.47/3.47	55.0	300	
YOKBOQ	FE/EE	3.66/3.59	3.45/3.46	54.4	300	

BTT

AHIXAS	EE	-/3.45,3.59	-	-	300	
CEYLOJ	FE/EE	3.70/3.37,3.37	3.46,3.34	44.7	123	
CEYLUP	FE/EE	3.68/3.35,3.35	3.43,3.32	44.4	93	
DONBEP	FE/EE	3.76/3.46,3.47	3.39,3.44,3.48	45.9	300	
DONBIT*	FE/EE	3.74/3.42,3.43	3.36,3.41,3.45	45.8	200	
DONBOZ	EE	-/3.57	-	-	300	
DONBUF	EE	-/3.53,3.56	-	-	100	
FOBBAA	EE	-/3.50	-	-	180	
GURQAM	FE/EE	-/3.44,3.44	3.36,3.38,3.49	44.0	113	
HOWFUV	FE	3.42,3.42	-	36.4	150	
IGOLIZ	-	-	-	-	180	
IXAQIH	EE	3.34,3.40,3.54	-	-	150	
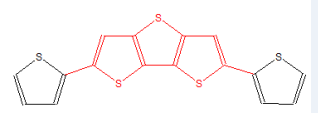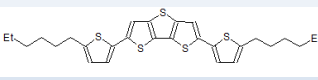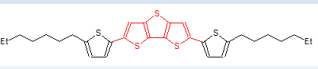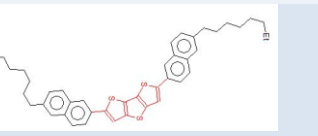
KEKCOT	FE	/3.45,3.45	3.76,3.78	50.6	300	
LISYOC	-	-	-	-	300	
LOCBAI	EE	3.57	-	-	100	
MOBGER	FE/EE	3.33/3.72	3.43	44.2	295	

Table S3 : CSD entries and shortest S···S, S···C distances, and herringbone angles.

Fig. S18 gives a histogram of the 78 unique hits of the herringbone of the thieno-thiophene motif in face-edge conformation (thus excluding the parallel face to face conformation). Only structures with S···C intermolecular contacts smaller than 3.6 Å (i.e. the sum of the Van der Waals radii of S and C + 0.1 Å) and with R<0.10 have been taken into account in the query, and face-edge angles beyond 10°. Each structure can contain more than one unique face-edge angle or shortest S···C distance. CSD refcode UROBUA (**BHH-BTBT** at 295 K) is shown as a red bin, thus appearing as a clear outlier among several others. Fig. S19 gives the shortest S···C distances for between thieno-thiophene motifs in face-edge mutual orientation. It is noted that the S···C distance of **BHH-BTBT** at 95 K is 3.309 Å, being thus at the extreme left side of the histogram. The scatter plot in Fig. S20 showing the S···C distance versus the FE or EE angle does not show a clear trend, the number of hits for FE S···C distances being more important than for EE S···C distances. Fig. S21-Fig. S23 analyze the behavior of the S···S distances as a function of the angle between thieno-thiophene angle. It seems that S···S contacts in EE orientation are in general more bonding than in FE orientation.
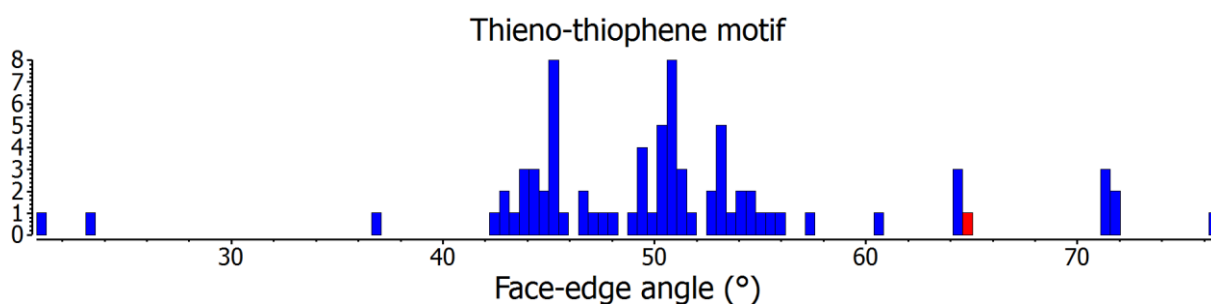
Fig. S18 : Histogram of the face-edge angle between thieno-thiophene motifs in face-edge orientation.

Thieno-thiophene motif

Fig. S19 : Histogram of the shortest S⋯C distances between thieno-thiophene motifs in face-edge mutual orientation.

Thieno-thiophene motif

Fig. S20 : Scatter plot of the shortest S⋯C distances versus the FE or EE angle between close thieno-thiophene motifs.
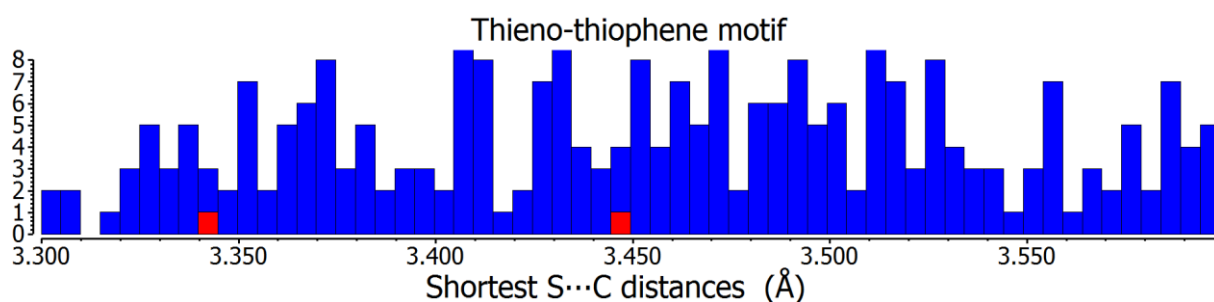
Fig. S21 : Histogram of the shortest S⋯S distances between thieno-thiophene motifs in edge-edge mutual orientation.

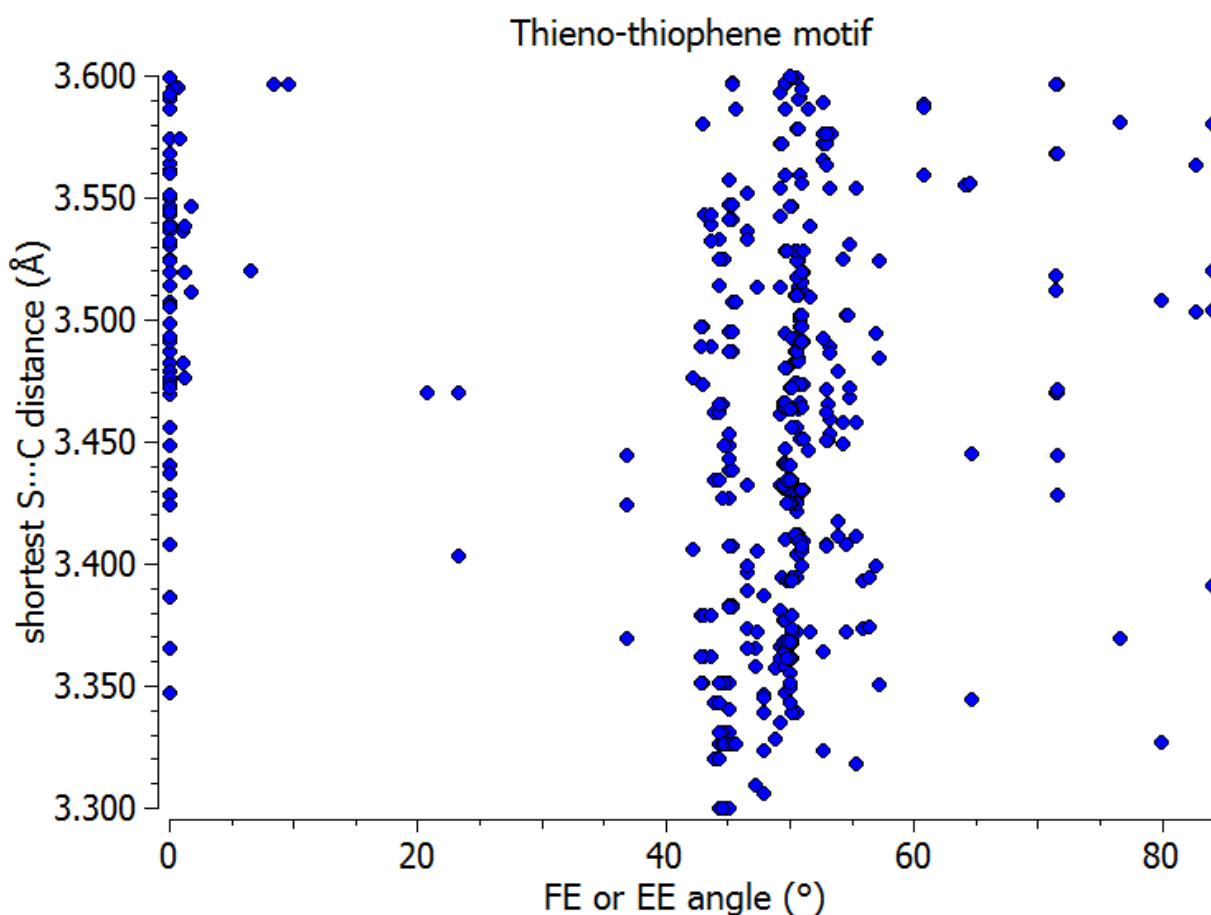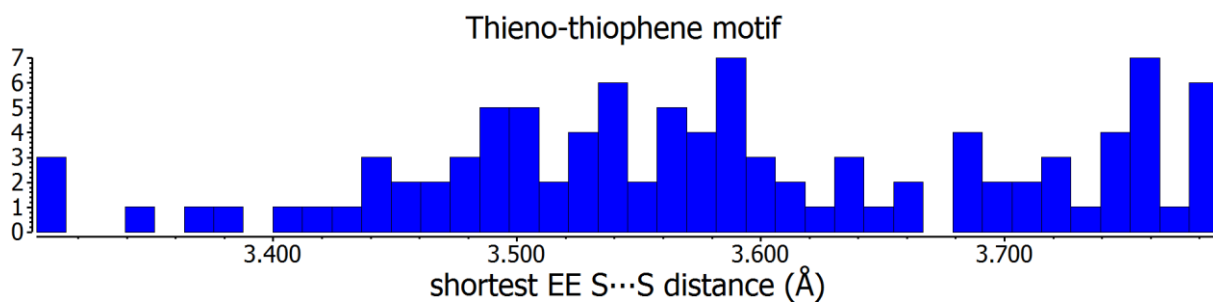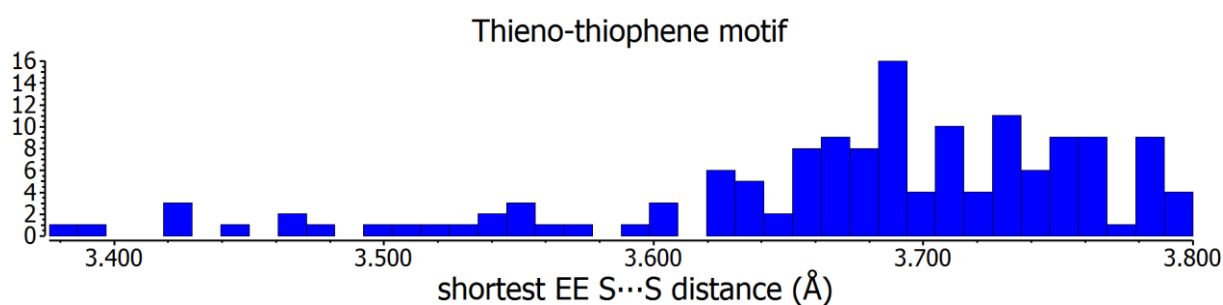**Fig. S22 :** Histogram of the shortest S⋯S distances between thieno-thiophene motifs in face-edge mutual (herringbone) orientation.
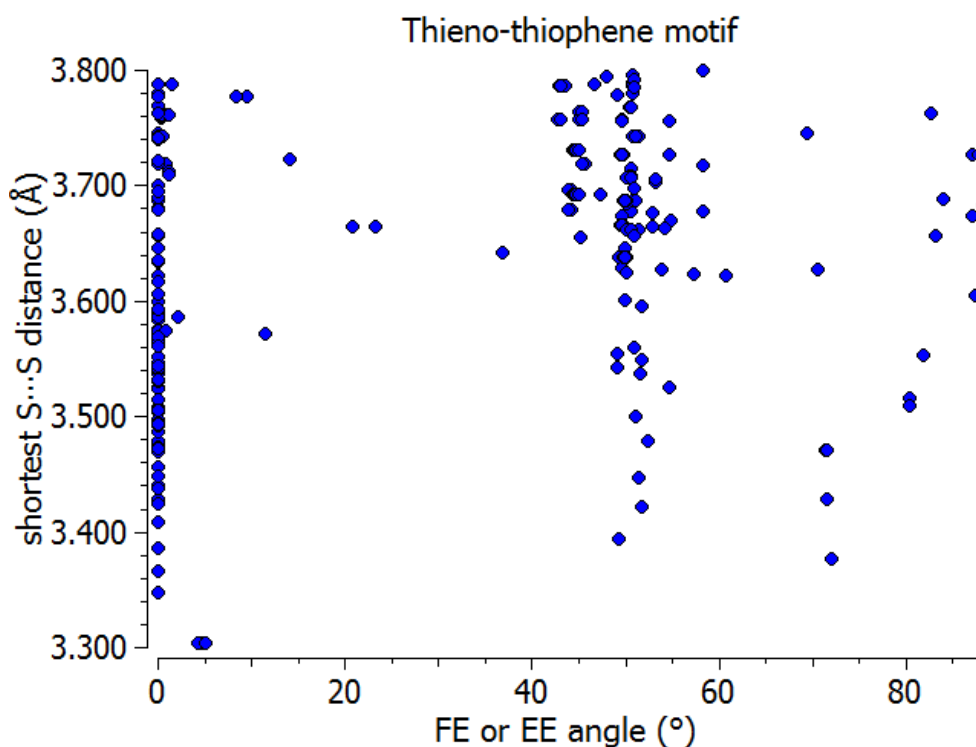

Fig. S23 : Scatter plot of the shortest S⋯S distances versus the FE or EE angle between close thieno-thiophene motifs.

Thermal expansion of C8-BTBT

Since thermal expansivity data are non-existent for BTBT derived compounds, we have carried out a determination of the cell parameter as a function of temperature for a compound which is closely related to **BHBH-BTBT**, i.e. **C8-BTBT**, in which the end OH groups are replaced by ethyl groups. We did not succeed in growing single crystals of **C6-BTBT** of sufficient quality for X-ray analysis. **C8-BTBT** was purchased from Aldrich and single crystals were obtained as described in described by Izawa *et al.* (*16*). **C8-BTBT** crystallizes as thin platelets as does **BHBH-BTBT**, but crystal quality is generally much better for **BHBH-BTBT** than for **C8-BTBT**. The cell parameters of **C8-BTBT** were determined at 125, 175, 225 and 275 K from approximately 450 reflections to 1.1 Å resolution. The ambient temperature cell parameters have been determined previously by Izawa *et al.* (*16*). Fig. S24 (right) gives the nominal cell parameters and Fig. S24 (left) the cell parameters normalized to their value at 125 K in the same setting $P2_1/a$ as was reported by Izawa *et al.*. The cell parameters are also tabulated in Table 4.

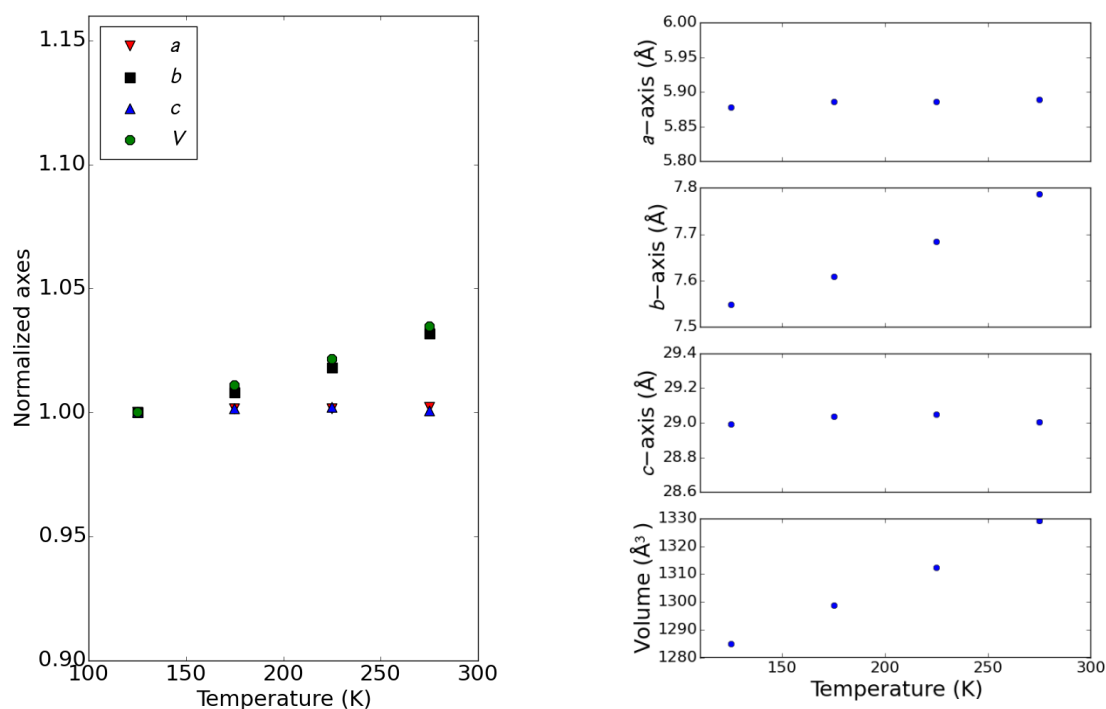**Fig. S24 :** Cell parameters of **C8-BTBT** normalized to their value at 125K (left) and on their nominal scale (right). The vertical scale of the left graph has been put at the same scale as the graph of the normalized cell parameters of **BHBH-BTBT** (Fig. 1 of the main manuscript). The estimated standard deviations of the nominal values are approximately at the same size as the symbols (see also **Table 4**)

T (K)	a (Å)	b (Å)	c (Å)	β (°)	V (Å³)
125	5.8780(11)	7.548(2)	28.991(7)	92.75(2)	1284.8(5)
175	5.8857(9)	7.6081(14)	29.037(6)	92.72(2)	1298.8(4)
225	5.8863(11)	7.6835(18)	29.049(8)	92.59(2)	1312.5(5)
275	5.8894(15)	7.787(2)	29.005(9)	92.31(3)	1329.2(7)

Table 4 : Cell parameters of **C8-BTBT** and their estimated standard uncertainties in parentheses. The room temperature (reported temperature 293 K) cell parameters of **C8-BTBT** as reported by xxx are 5.927(7) Å, 7.88(1) Å, 29.18(4) Å, β=92.443(4), V=1362(3) Å³. It is noted that the four temperature dependent cell parameter determinations on **C8-BTBT** have been effectuated on the same crystal.

A complete structure determination was carried out at 175K, which allowed determining the face-edge herringbone angle to be 52.6°, whereas at room temperature it is 55.0°. In comparison, for **BHH-BTBT** this angle is 56.7° at 175K and 64.9° at 295K.

Comparison of the structures of C8-BTBT and BHH-BTBT

The crystal packings of **C8-BTBT** and **BHH-BTBT** are very similar in the sense that they are composed of herringbone-arranged **BTBT** cores (Fig. S25); the difference is that the aliphatic side chains are differently oriented in both structures. Fig. S26 shows how the herringbone-packed layers stacking, with a hydrophobic van der Waals gap between different layers in **C8-BTBT** and a hydrogen bonded network between alternating layers in the structure of **BHH-BTBT**. The relative orientation of the **BTBT** cores in the two structures is shown in Fig. S27. The two structures differ by the opposite orientation of the tilted **BTBT** core with respect to the neighboring **BTBT** core, i.e. the tilted core is rotated by 180° around the long axis of the core with respect to the orientation of the other tilted core. This makes, as was outlined by Roche et al, that the density of close contacts in **C8-BTBT** is twice of that in **BHH-BTBT**, but that the close contacts in **BHH-BTBT** are on the average shorter than those in **C8-BTBT**.

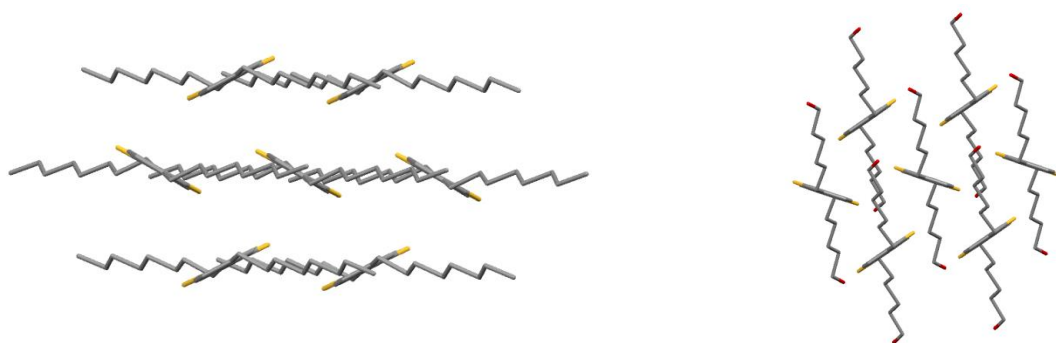**Fig. S25 :** Comparison of the herringbone stacking of the **BTBT** cores in the structure of **C8-BTBT** (left) and that in the structure of **BHH-BTBT** (right).
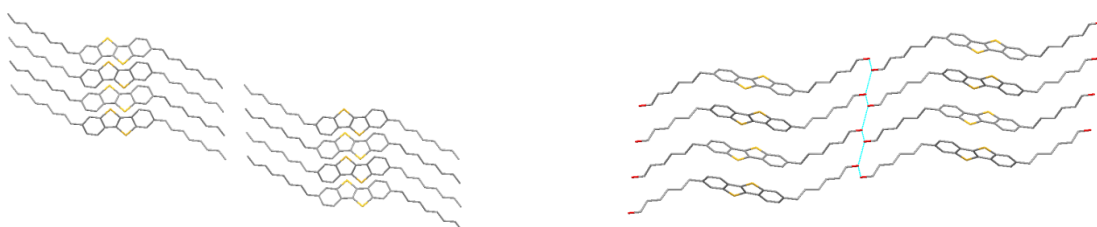

Fig. S26 : Comparison of the stacking of the aliphatic layers in the structure of **C8-BTBT** (left) and that in the structure of **BHH-BTBT** (right), where the hydrogen-bonded network in the structure of **BHH-BTBT** is indicated with blue lines.
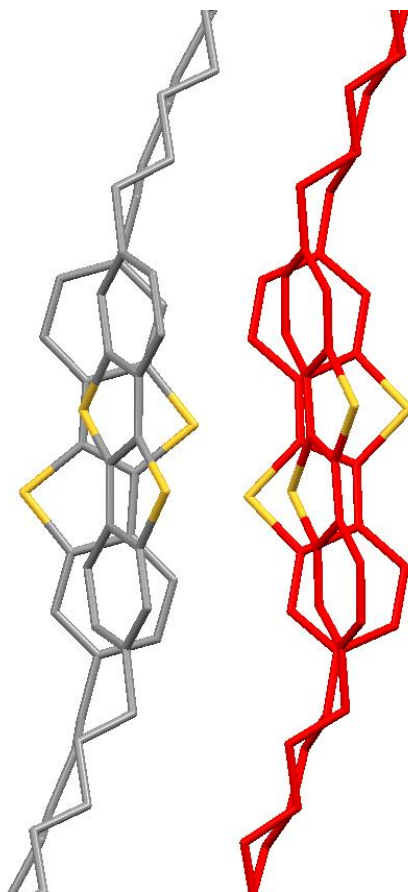
Fig. S27 : Comparison of the relative positioning of neighboring face to edge **BTBT** cores in the structures of **BHH-BTBT** and **C8-BTBT**. The carbons of the former structure are in grey and those of the latter in red.

2. DFT Calculation Method and *ab initio* lattice dynamics

The computation of very soft materials such as **BHH-BTBT** with a cohesive energy mostly dominated by van der Waals forces, at finite temperature is still a great challenge. It implies using a van der Waals functional (PBE+D3 in the present case) that were mostly only evaluated for very low temperature (0K) combined with *ab inito* dynamics that are limited for standard calculations to a 10 ps order of magnitude preventing an extensive description of the phase space mostly because of CPU time limitations. Therefore, it was not clear if advanced DFT-based dynamics can give some insight into finite temperature behavior of such a complex compound.

A 248-atom unit cell, $C_{104}H_{128}O_8S_8$, was used to compute the **BHH-BTBT** structures at different temperatures. Periodic electronic structure calculations were performed using density functional theory (DFT) within the PBE+D3 generalized gradient approximation, including van der Waals

contributions. We have used projected augmented wave (PAW) pseudopotentials (*17*), (*18*) as implemented in the VASP code (*19*), (*20*). A Γ-centered $2 \times 3 \times 1$ *k*-point mesh with the high *k*-point density in the direction of the smallest unit-cell parameter was used. **BHH-BTBT** structures were computed using a 550 eV cut-off (to account for the more electronegative oxygen and sulphur atoms and properly describe electronic polarization) with both the atomic positions and the unit cell being optimized. For the 0K optimization, the residual forces on atoms are lower than 0.01 eV.Å^{-1} and the unit cell parameters were fully optimized to zero the unit cell stress tensor. The finite temperature was obtained by mean of a Parrinello-Rahman dynamics in connection with a Langevin thermostat within the NPT ensemble by coupling the Parrinello and Rahman equations of motion (*21*), (*22*) for both atomic and lattice degrees of freedom and a Langevin thermostat (*23*). The time step for the dynamic was chosen to 0.5 fs as smaller 0.25 fs time steps are leading to similar results. The 0K calculation was optimized from the experimental 95K X-ray structure. The 295 K calculation was obtained using the experimental 295 K X-ray structure as a starting point and using five different random roots as a starting points leading to five different dynamics we have for 12 ps each and we have averaged the geometry over these 5 dynamics. These dynamics tends to accumulate around two different attractors in the phase space (designed as α and β domains) as explained below. The 235 K was done similarly starting from the computed 295 K (from two limit α and β domains) and cooling it to 235 K.

The other temperatures were obtained by cooling down the final 295 K structure to 235 K, 175 K 95 K and warming it up to 350 K For each temperature the trajectories were thermalized for 2ps and then were propagated for at least 8 ps more and the average parameters were extracted (average lattice values and atomic positions). It should be noted that the warming of the 0K calculation as a starting point leads to another polymorphic structure with a different thermal behavior, that is iso-energetic (within a few tenth of eV/unit cell) with the one computed from the experimental data suggesting that two polymorphs exist at finite temperature but collapse into one structure at 0K.

First, we have computed the fully optimized structure at 0 K. For comparison, we have extrapolated a 0K-experimental unit cell using the linear thermal expansion seen in experimental samples in the 95-200 K range. The experimental extrapolated value are within 1.3% of the computed ones (a_{exp}=7.51 Å; a_{theo}=7.61 Å (1.3%); b_{exp}=6.04 Å; b_{theo}=5.99 Å (0.9%), c_{exp}=49.04 Å; c_{theo}=49.32 Å (0.6%) and V_{exp}=2216.8 Å^3; V_{theo}=2222.6 Å^3 (0.3%)). The BPE+D3 functional is then giving a very good quality 0K-structure in full agreement with the experimental one.

The β structure can be optimized at 0K and gives a structure different from the α-0K structure (mostly by the rotation of the BTBT moieties) suggesting that the two structures corresponds to two different local polymorphs. The small structural difference nevertheless is associated to quite different band structure (as seen in Fig. S31).

The energy of α-0K including zero point energy (from harmonic vibrational calculations) is about 340 meV (1.4 meV/atom) more stable than the β-0K explaining that it is the dominant structure at low temperature. At higher temperature both phases become competitive as the β phase has more low energy phonons. Therefore a α to β phase transform could have been expected from purely harmonic calculations around 300 K. Nevertheless, in the present case it should be noticed that the harmonic extrapolation is a rather poor approximation.

We have also investigated theoretically the two possible orientations of the O-H bonds that are not possible to differentiate experimentally. The two different orientations lead to a tiny energy difference of 20 meV/unit cell. Nevertheless, during the dynamics duration, no orientation inversion is observed in the OH-array suggesting that the inversion is associated with a (relatively) large activation barrier. This could be understood as the H-bond network is unidimensional (as seen in Fig. S3) the change of orientation would need the full breaking of a H bond and the reorientation of one OH bond before the other OH reorientation can proceed resulting in an important energy barrier (at least of the order of 1 H-bond). This explains that no change in the H-bond network orientation is observed in our limited dynamic time.

	α_V	α_a	α_b	α_c	$a{\times}b$	$\Delta\beta$	Δ(G1)	Δ(G2/G3)
x-ray	248(19)	441(20)	-274(8)	81(5)	144(14)	-159(7)		
DFT	173(9)	348(72)	-216(64)	49(8)	95(8)	-152(23)	-0.4	-1.1

Table S5 Average linear thermal expansion coefficients from DFT calculations compared to experimental X-ray values. Expansion coefficients are in $10^{-6}K^{-1}$ whereas the gap variations Δ(G1) and Δ(G2/G3) are in meV.K^{-1}. The linear thermal expansion coefficients were calculated using the expression $l=l(T_0)+\alpha_i*T$ between T_0 and T_1. T_0 is 0 K for the DFT data and 95 K for the x-ray data. T_1 is 295 K in both cases. Note that the real expansivity is not linear (**Fig. S7**), but that the coefficients have been calculated in this way in order to make a better comparison with data from the literature.

Structure	α-0K	α-95K	α-175K	α-235K	β-235K	α-295K	β-295K
ϕ_{sym}(%)	0.18	0.19	0.59	0.60	12.44	0.86	1.41

Table S6 : Symmetry agreement factors ϕ_{sym} of the *P1* DFT structures with respect to the symmetry operators of the experimental space group *I*2/*a*.

The dynamics at different temperature were done and corresponding trajectories in (a,b) unit cell parameters are given in Fig. 4 of the main manuscript. In this representation a clear correlation between the *a* and *b* cell parameters is observed (while *a* increases, *b* tends to decrease) showing that the massive positive and negative thermal expansion are linked. With increasing temperature, the trajectories shows the same *a/b* correlation but dispersion around the OK position becomes larger and larger in a non symetric manner with larger *a* favored upon smaller *a* (resp. smaller *b* favored upon larger ones).

Above 200 K, the trajectories can be in two different domains corresponding to α and β. Therefore the total average structure has to be averaged on both domains leading to a strong increase of the thermal expansion properties. Therefore the total structure has to be averaged on both domains leading to a strong increase of the thermal expansion properties. At 295 K, the fluctuation of the a parameter is so large that it becomes more abritaty to defined to α and β domains even for a simulation time of 10 ps.

Table S6 gives the symmetry agreement factors ϕ_{sym} (*24*) of the *P1* DFT structures with respect to the symmetry elements of the experimental *I*2/*a* structure. A symmetry agreement factor of 0% means that the electron density in the *P1* map perfectly matches a *I*2/*a* space group symmetry whereas a symmetry agreement factor of 100% means that the match is completely random. It is noted that besides the calculation of the symmetry agreement factor also the symmetrized DFT electron density map can be obtained (*3*) with the program *SUPERFLIP* in 'perform symmetry' mode using the keywords 'searchsymmetry average' and 'derive symmetry use' with 'modelfile *DFT.cif*' , followed by atom assignment using the program *EDMA* (*25*). Then the symmetrized DFT structure *DFTsym.cif* can be compared to the experimental file *exp.cif* in a new Superflip run in 'perform symmetry' mode with the two instructions 'referencefile *exp.cif*' and 'modelfile *DFTsym.cif*' .
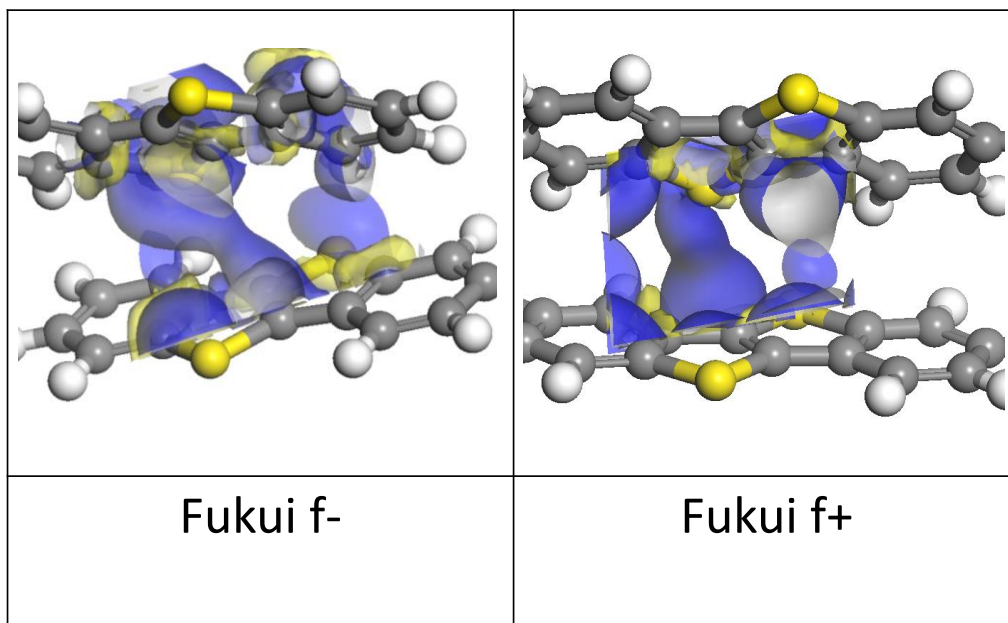
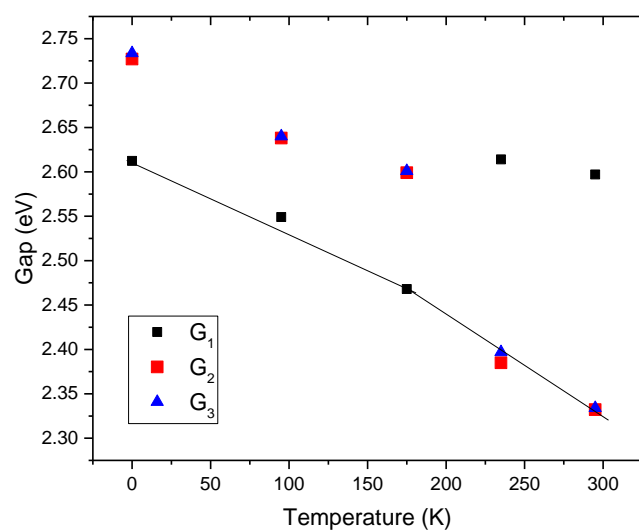**Fig. S28 :** f⁻ and f⁺ Fukui functions for **BHH-BTBT**

Fig. S29 : Evolution of the vertical gap with temperature for the $G1\left(\frac{1}{4}, 0, 0\right)$, $G2\left(\frac{1}{4}, \frac{1}{3}, 0\right)$, and $G3\left(-\frac{1}{4}, \frac{1}{3}, 0\right)$ irreducible *k*-points.
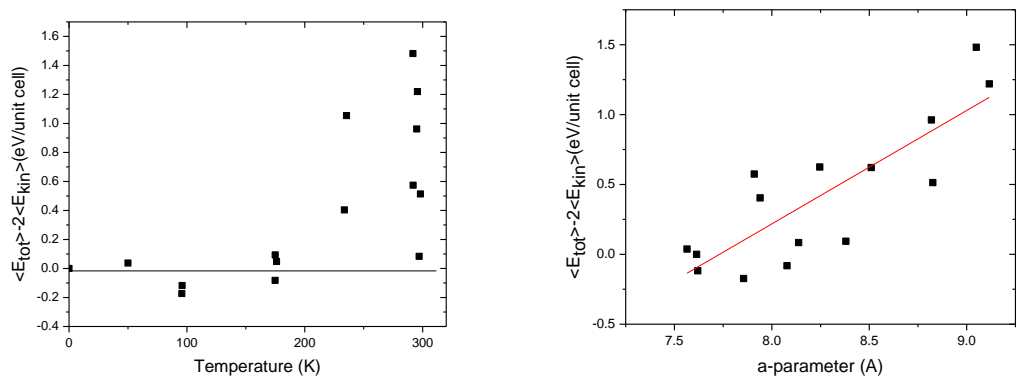
Fig. S30 : $\langle E_{tot} \rangle - 2\langle E_{kin} \rangle$ per unit-cell computed for different trajectories at different temperatures, and *a*-parameter dispersion as a function of $\langle E_{tot} \rangle - 2\langle E_{kin} \rangle$.
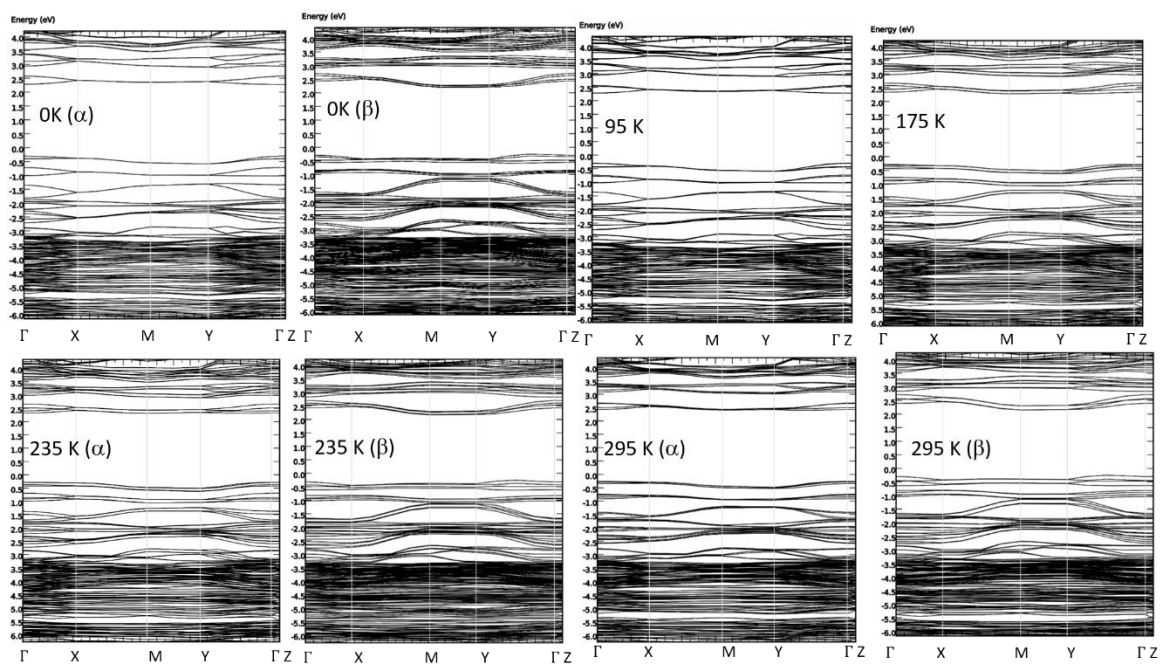

Fig. S31: Band structure for the α and β phases of the 0 K, 235 K, and 295 K structures and for the average structure at 95 K and 175 K.

Comparison of high-temperature DFT structures

As is visualized in Fig. 4 of the main manuscript the high-temperature DFT structure has two different branches α and β. The structures at 235 K and 295 K have been averaged in each branch and are compared in Table 1 of the manuscript, together with the experimental structures at those temperatures.

Fig. S32 gives the best overlay of the α and β averaged DFT structures at 295 K, as calculated with Mercury (*26*).
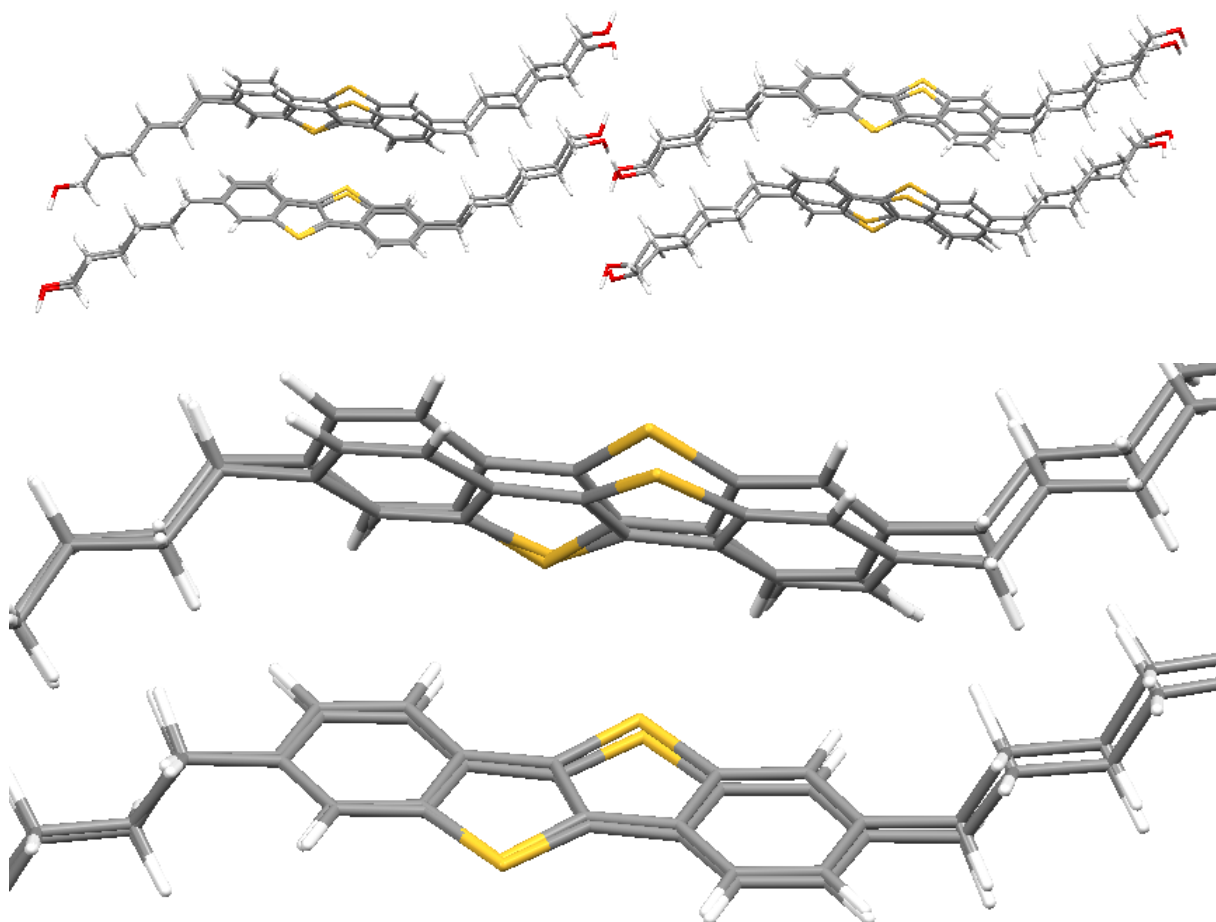

Fig. S32 : Best overlay of the α and β DFT structures at 295 K. The bottom figure is a zoom of the top figure.

3. UV-vis spectroscopy for BHH-BTBT and C8-BTBT

UV-vis spectra were performed on a SAFAS UVMC2 spectrometer with 1 nm resolution. Experiments were realized on single crystals. **BHH-BTBT** single crystals were obtained as described in Roche *et al.* (*1*). **C8-BTBT** was purchased from Aldrich and single crystals were obtained as described in described by Izawa *et al.* (*16*). Single crystals were placed between two quartz slides and stuck with carbon tape on a cold finger cooled by liquid nitrogen and placed under vacuum in a cryostat (Fig. S33).
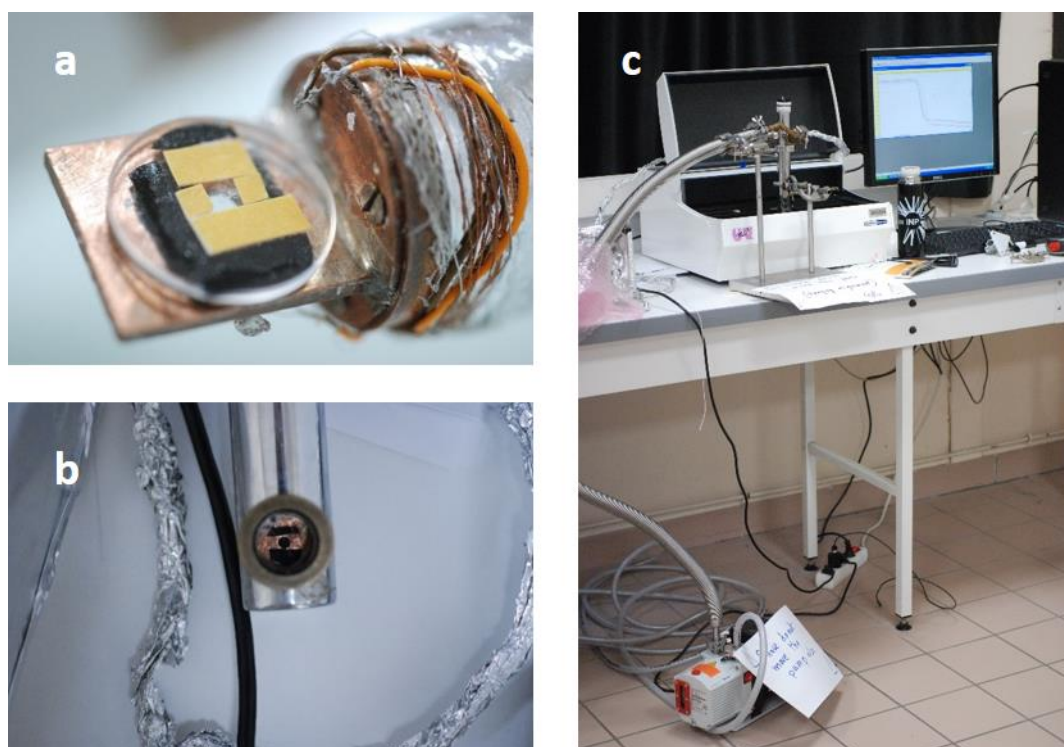

Fig. S33 a) single crystals placed between two quartz slides b) hole letting UV-vis or IR beams for measurements c) Experimental set-up used to record UV-vis absorption as a function of the temperature.

UV-vis absorption spectra of crystals of **BHH-BTBT** and of **C8-BTBT** were recorded as a function of the temperature from 100 k to 296 K. Measurements were performed 15 minutes after reaching the required temperature to overcome temperature homogenization issues. A first UV-vis spectrum was recorded at room temperature (296 K pristine) and the samples were cooled to 100 K. increasing the temperature from 100 K to 296 K spectra were recorded each 20 K for **BHH-BTBT** (**Fig. S34**) and each 50 K for **C8-BTBT** (Fig. S35). At each temperature, the optical band gap was estimated to be located at the edge-band ($E_{GAP}T$ K) of the UV-vis spectrum. Finally, we controlled that the room temperature absorption spectrum remained unchanged after the thermal treatment of the samples: $EGAP_{296}$ K remained unchanged after the cooling-heating cycle in both cases (**Fig. S34** and Fig. S35). The variation of the optical band gap has been reported on figure S37 plotting ($E_{GAP}T$ K - $E_{GAP}296$ K) as a function of T. The slopes of the curves (meV.K^{-1}) were calculated by linear fitting. (Figure S37).

In the case of **C8-BTBT**, the band gap remained stable in the temperature range 100 - 300 K which is consistent with band like conduction observed by Cho et al. (*27*) (Fig. 4 of main manuscript, blue curve)

However, in the case of **BHH-BTBT**, the optical bandgap was dramatically affected by the temperature. The $E_{GAP}T$ K decreased linearly from 100 to 300 K with a slope change at 210 K.
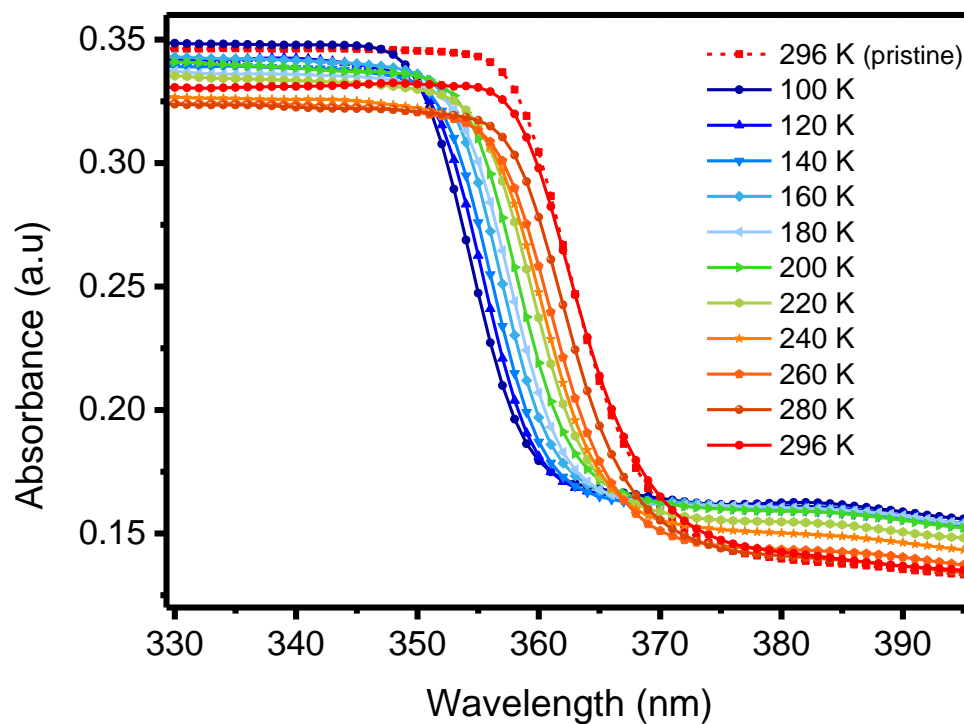

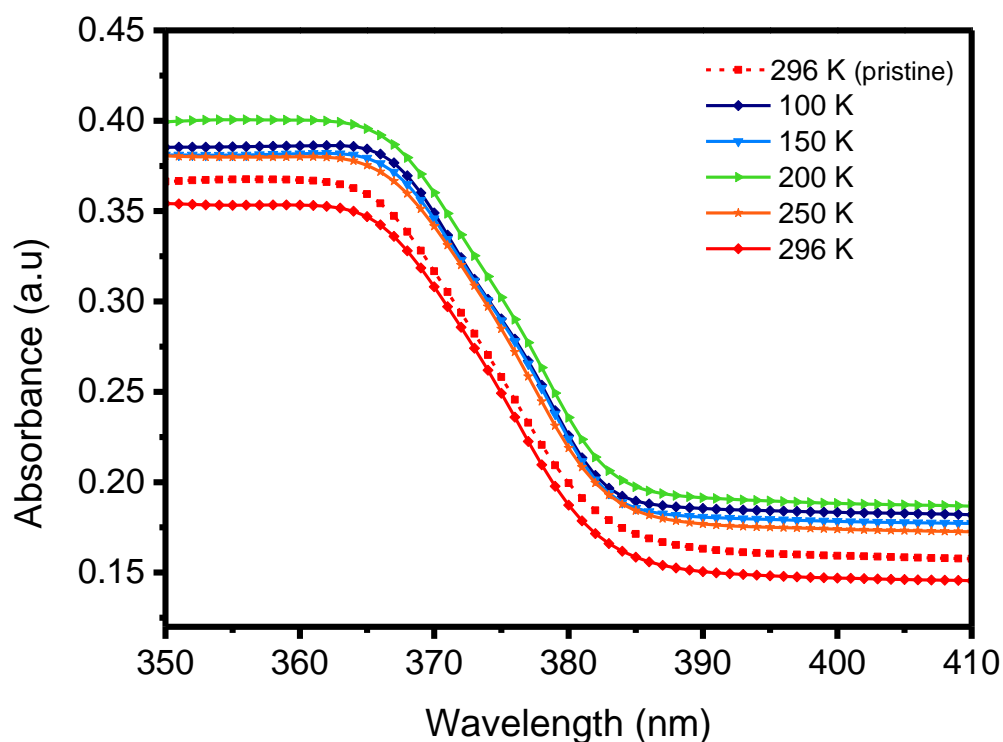**Fig. S34** : UV-vis absorbance of BHH-BTBT as a function of temperature

Fig. S35 : UV-vis absorbance of **C8-BTBT** as a function of temperature

4. Differential Scanning Calorimetry measurements

Differential scanning calorimetry (DSC) traces were obtained on a DSC 200 F3 Maia from Netzsh at 10 K/min. (Fig. S36) Scanning from 140 K to 300 K, crystals of **BHH-BTBT** exhibit one endothermic phase transition at 209.1 K (first heating) and 209.2 K (second heating) and one exothermic transition during the cooling at 171.3 K (first cooling) and 187.6 K (second cooling)

The energies involved in those transitions are very low: 45 J/mol for the exotherms and 200 J/mol for the endotherms.
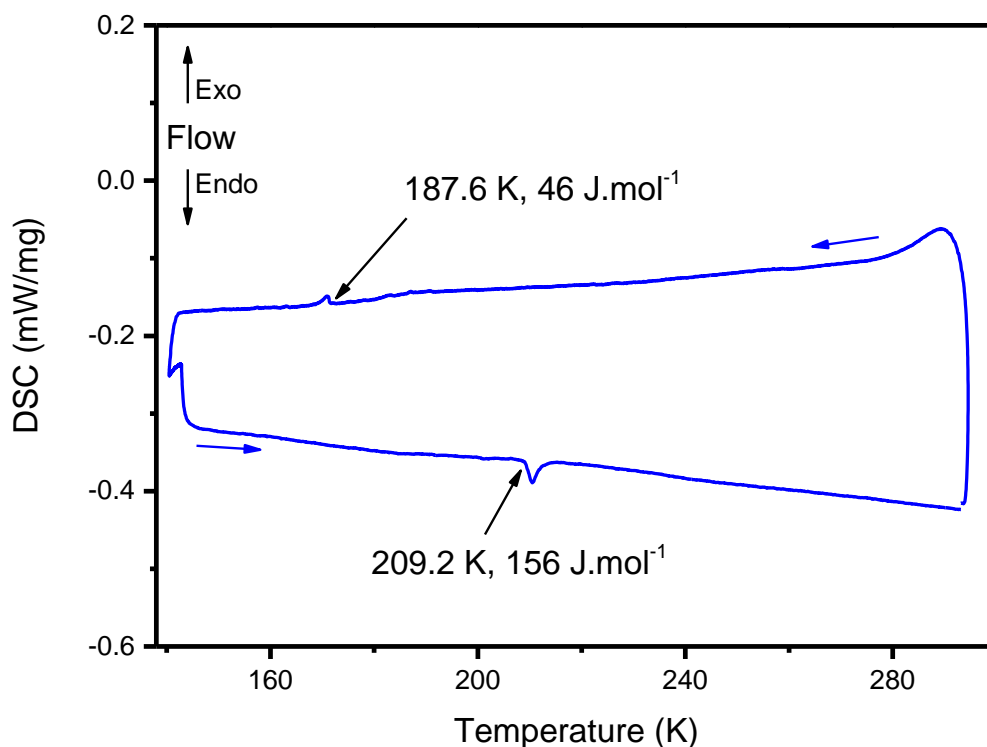
Fig. S36: DSC profiles of the heating and cooling cycle (10°K/min) from 140 K to 300 K realized on **BHH-BTBT** crystals. Two events are observables: one exothermic transition during cooling at 187.6 K and one endothermic during heating at 209.2 K.

5. NTE Microscopy pictures.

Microscopy pictures (Fig. S37) were obtained on a Zeiss Axio Imager-A1 microscope equipped with a Nikon D90 camera and a Linkam temperature controlled stage. The Linkam temperature stage allows sample temperatures ranging from -196°C up to 600°C. The **BHH-BTBT** single crystal was placed under vacuum on a Fraunhofer Si n-doped substrate covered by 230 nm of SiO_2 as insulator. To avoid any interaction between the crystal and the subtract, silicon oxide was pretreated with trichloro(1H,1H,2H,2H-perfluorooctyl)silane (FTS). Even if the Linkam stage was placed under vacuum, residual traces of water could be observed as tiny black spots at 100K. They disappeared during the temperature rising .
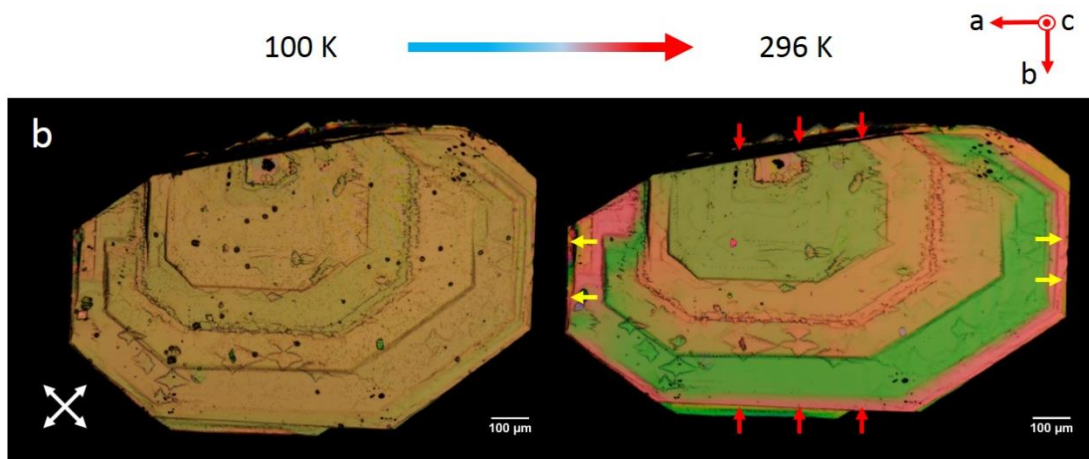
Fig. S37: Direct observation of the modification of the size of a **BHH-BTBT** single crystal from 100 K to 296 K by cross-polarized optical microscopy. NTE (Red arrows), PTE (yellow arrows).

References

1. Roche, G. H.; Tsai, Y.-T.; Clevers; Thuau, D.; Castet, F.; Geerts, Y. H.; Moreau, J. J. E.; Wantz, G.; Dautel, O. J. The role of H-bonds in the solid state organization of [1]benzothieno[3,2-b][1]benzothiophene (BTBT) structures: bis(hydroxy-hexyl)-BTBT, as a functional derivative offering efficient air stable organic field effect transistors (OFETs). *J. Mater. Chem. C 4* **2016,** 6742.

2. Rigaku Oxford Diffraction. CrysAlis PRO. Rigaku Oxford Diffraction, Yarnton, Oxfordshire, England,. **2011**.

3. Palatinus, L.; Chapuis, G. SUPERFLIP–a computer program for the solution of crystal structures by charge flipping in arbitrary dimensions. *J. Appl. Crystallogr.* **2007,** *40,* 786.

4. Betteridge, P. W.; Carruthers, J. R.; Cooper, R. I.; Prout, K.; Watkin, D. J. CRYSTALS: software for guided crystal structure analysis. *J. Appl. Crystallogr.* **2003,** *36,* 1487.

5. Dolomanov, O. V.; Bourhis, L. J.; Gildea, R. J.; Howard, J. A. K.; Puschmann, H. OLEX2: a complete structure solution, refinement and analysis program. *J. Appl. Cryst.* **2009,** *42,* 339-341.

6. Momma, K.; Izumi, K. VESTA 3 for three-dimensional visualization of crystal, volumetric and morphology data. *J. Appl. Cryst.* **2011,** *44,* 1272-1276.

7. Ogborn, J. M.; Collings, I.; Moggach, S. A.; Thompson, A. L.; Goodwin, A. L. Supramolecular mechanics in a metal–organic framework. *Chem. Sci.* **2012,** *3,* 3011-3017.

8. Garnier, P.; Calvarin, G.; Weigel, D. Determination of thermal expansion tensors by X-ray diffraction: II-Expansion of lead oxides and interpretation as a function of their structure and chemical bonds. *J. Chim. Phys. Phys.-Chim. Biol.* **1972,** *11-12,* 1711-1718.

9. Weigel, D.; Beguemsi, T.; Garnier, P.; Bérar, J. F. Evolution des tenseurs de dilatation thermique en fonction de la temperature. I. Loi generale d'evolution de la symetrie du tenseur. *J. Solid State Chem.* **1978,** *23,* 241-251.

10. Spek, A. L. Structure Validation in Chemical Crystallography. *Acta CRyst. D* **2009,** *65,* 148-155.

11. Cliffe, M. J.; Goodwin, A. L. PASCal: a principal axis strain calculator for thermal expansion and compressibility determination. *J. Appl. Cryst.* **2012,** *45,* 1321-1329.

12. Bürgi, H.-B.; Rangavittal, N.; Hauser, J. Molecular Motions in Crystalline An. *Helv. Chim. Acta* **2001,** *84,* 1889-1906.

13. Schomaker, V.; Trueblood, K. N. On the rigid-body motion of molecules in crystals. *Acta Cryst. B* **1968,** *24,* 63-76.

14. Dunitz, J.; Schomaker, V.; Trueblood, K. N. Interpretation of atomic displacement parameters from diffraction studies of crystals. *J. Phys. Chem.* **1988,** *92,* 856-867.

15. Groom, C. R.; Bruno, I. J.; Lightfoot, M. P.; Ward, S. C. The Cambridge Structural Database. *Acta Cryst. B* **2016,** *72,* 171-179.

16. Izawa, T.; Miyazaka, E.; Takimiya, K. Molecular Ordering of High-Performance Soluble Molecular Semiconductors and Re-evaluation of Their Field-Effect Transistor Characteristics. *Adv. Mater.* **2008,** *20,* 3388-3392.

17. Blöchl, P. E. Projector Augmented-Wave Method. *Phys. Rev. B* **1994,** *50,* 17953-17979.

18. Kresse, G.; Joubert, D. From Ultrasoft Pseudopotentials to the Projector Augmented-Wave Method. *Phys. Rev. B* **1999,** *59,* 1758-1775.

19. Kresse, G.; Furthmuller, J. Efficiency of Ab-Initio Total Energy Calculations for Metals and Semiconductors Using a Plane-Wave Basis Set. *Comput. Mater. Sci.* **1996,** *6,* 15-50.

20. Kresse, G.; Hafner, J. Ab-Initio Molecular-Dynamics Simulation of the Liquid-Metal Amorphous-Semiconductor Transition in Germanium. *Phys. Rev. B* **1994,** *49,* 14251-14269.

21. Parrinello, M.; Rahman, A. Crystal Structure and Pair Potentials: A Molecular-Dynamics Study. *Phys. Rev. Lett.* **1980,** *45,* 1196-1199.

22. Parrinello, M.; Rahman, A. Polymorphic transitions in single crystals: A new molecular dynamics method. *J. Appl. Phys.* **1981,** *52,* 7182-7190.

23. Allen, M. P.; Tildesley, D. J. *Computer simulation of liquids;* Oxford university press: New York, 1991.

24. Palatinus, L.; van der Lee, A. Symmetry determination following structure solution in P1. *J. Appl. Cryst.* **2008,** *41,* 975-984.

25. Palatinus, L.; Prathapa, S. J.; van Smaalen, S. EDMA: a computer program for topological analysis of discrete electron densities. *J. Appl. Cryst.* **2012,** *45,* 575-580.

26. Macrae, C. F.; Bruno, I. J.; Chisholm, J. A.; Edgington, P. R.; McCabe, P.; Pidcock, E.; Rodriguez-Monge, L.; Taylor, R.; van de Streek, J.; Wood, P. A. Mercury CSD 2.0 - New Features for the Visualization and Investigation of Crystal Structures. *J. Appl. Cryst., 41* **2008,** *41,* 466-470.

27. Cho, J.; Higashino, T.; Mori, T.; Appl. Phys. Lett. 106, 1. (. Band-like transport down to 20?K in organic single-crystal transistors based on dioctylbenzothienobenzothiophene. *Appl. Phys. Lett.* **2015,** *106,* 193303.